

Impulse Approximation limitations to the
($e, e'p$) reaction on ^{208}Pb , identifying
correlations and relativistic effects in the
nuclear medium

K. A. Aniol(spokesperson), M. B. Epstein, D. J. Margaziotis
California State University, Los Angeles, CA 90032

J. M. Udias(spokesperson)
Universidad Complutense de Madrid, Madrid, Spain

D. Higinbotham, C.W. de Jager, J. Leroze, B. Reitz(spokesperson),
A. Saha¹(spokesperson), E. Voutier
Jefferson National Accelerator Facility, Newport News, VA 23606

O. Gayou, S. Gilad
Massachusetts Institute of Technology, Cambridge, MA 02139

P. E. C. Markowitz
Florida International University, Miami, FL 33199

R. Lindgren
University of Virginia, Charlottesville, VA 22901

Simon Sirca
University of Ljubljana, Slovenia

F. Garibaldi, E. Cisbani, F. Cusanno, S. Frullani
Gr. Coll. Sanita, INFN Roma1, Italy

G. M. Urciuoli
INFN Roma1, Italy

R. De Leo, L. Lagamba, S. Marrone
INFN Bari, Italy

Ron Gilman
Rutgers University, Piscataway, NJ 08855

and the Hall A Collaboration

June 27, 2005

¹Contact person, (757) 269-7605, saha@jlab.org

Abstract

This measurement will determine the TL asymmetry, A_{TL} , for protons emitted forward of the three momentum transfer \mathbf{q} and backward of \mathbf{q} as a function of missing momentum, p_{miss} for the reaction $^{208}\text{Pb}(e, e'p)^{207}\text{Tl}$. The low lying states in ^{207}Tl will be the focus of this study using the high resolution spectrometers of Hall A. In the range of missing momenta $p_{miss} < 300$ MeV/ c a complex structure in A_{TL} is predicted within the impulse approximation. Relativistic mean field calculations predict values of A_{TL} that deviate substantially from the predictions that do not include the enhancement of the lower component of the wave function due to dynamical relativistic effects. Spectroscopic factors will also be extracted for these low lying states and they will be compared to the ones derived at lower Q^2 to establish a dependence, or lack thereof, on Q^2 . Cross section measurements will also be extended out to 500 MeV/ c in missing momentum. An excess of strength at high p_{miss} has been found in a former experiment, that has been alternately attributed to long range correlation using nonrelativistic analyses, or to relativistic effects from a full relativistic analysis. This measurement will be made in fixed \mathbf{q}, ω kinematics, $q=1$ GeV/ c , $\omega = 0.433$ GeV, $Q^2 = 0.81$ (GeV/ c)². This is the first measurement of the (e,e'p) reaction in lead done at constant (\mathbf{q}, ω) and under quasielastic conditions, $x_B = 1$. These data will provide observables for current and future theories of long range correlations and dynamical relativistic effects in the nuclear medium.

Contents

1	Goals and Physics Motivation	3
1.1	Introduction and Goals	3
1.2	Physics Motivation	9
1.3	Choice of Lead as a Target	10
1.4	Chasing Correlations	12
2	Relation to other JLab Proposals	14
3	Theoretical Predictions	20
4	Kinematics and Experimental Rates	25
4.1	Experimental Setup	25
4.2	Proposed Kinematics	28
4.3	Singles Rates	28
4.4	Coincidence Rates	29
4.5	Systematic and Statistical Uncertainties	29
5	Expected Results	31
6	Summary and Beam Time Request	39
6.1	Summary	39
6.2	Beam Time Request	39
A	Kinematics	41
B	Target Issues and Simulation of Results	43
B.1	Lead Target Test	43
B.2	Target Development and Geant Simulations	46
B.2.1	Thin Target GEANT Simulation in flowing LH ₂	46

B.2.2	Simulation using the NIKHEF Geometry	49
B.2.3	Simulation using a Diamond–Lead Foil Sandwich . . .	50
B.2.4	Calibration of Missing Mass Spectrum with Bismuth .	52

Chapter 1

Goals and Physics Motivation

1.1 Introduction and Goals

The question we wish to address in this measurement is “ How well do we understand nuclear structure? ”. The nucleus is a dense system of fermions whose motion to first order can be treated as independent particles moving in a mean field. However, deviations from independent particle motion for orbits near the Fermi energy are clearly present and are attributed to various correlations. Changes in the occupation probability of mean field orbits and in the momentum distribution, especially above the Fermi momentum, have been attributed in prior experiments and nonrelativistic analyses to these correlations. On the other hand, is there really excess strength in the momentum distribution at high p_{miss} for these states near the Fermi energy? A relativistic treatment of the bound and free nucleon states shows no deviation from an independent particle model prediction. The asymmetry A_{TL} , accessible in $(e, e'p)$ reactions, is a relatively new and as yet little exploited observable for low lying excited states. It is sensitive to the theoretical approach employed and is of prime interest in this measurement.

Coincidence measurements at quasielastic conditions have been a source of information on momentum distributions and other single-particle properties of nucleons in nuclei. With the advent of the Jefferson Lab facility, the range of missing momentum that can be explored in quasielastic kinematics was extended well beyond the previous experiments mostly done at NIKHEF and Saclay. The physics program in Hall A at Jefferson Lab commenced in the summer of 1997 with a detailed investigation of the $^{16}\text{O}(e, e'p)$ reaction

in quasielastic, constant (q, ω) at q near 1 GeV/c [1]. This experiment explored for the first time missing momenta at and beyond 300 MeV/c with $x_B = 1$. In this region, where the mean field momentum distributions are expected to be small, experiments should be sensitive to short and long range correlations, mesons exchange currents (MEC), relativistic effects (RE) and final state interactions (FSI).

In the past, the high missing momentum region of the $(e, e'p)$ reaction has been explored for ^{12}C (Mainz [2]), ^{16}O (JLab [3, 4] and ^{208}Pb (NIKHEF [5]). But only at JLab, thanks to the larger Q^2 available, relatively high missing momentum can be achieved at quasielastic ($x_B = 1$) conditions.

It has been claimed [6, 7], from the comparison of $(e, e'p)$ data in ^{12}C at different momentum transfers, that the spectroscopic factors as measured in $(e, e'p)$ reactions at exclusive conditions display a dependence on the momentum transfer. This dependence would saturate at Q^2 of around 1 (GeV/c)² [7]. However, it has recently been pointed out [8] that the influence of short range correlations on the determination of the spectroscopic factors was handled differently between the low q and high q measurements. Moreover, subsequent studies on ^{16}O including data from 0.2 to 0.8 (GeV/c)² did not find evidence for such Q^2 dependence (see for instance ref. [9] and Fig. 1.1).

^{208}Pb has been studied via $(e, e'p)$ at moderate momentum transfer in the past and reliable spectroscopic factors have been determined ([13, 14, 15] see also Fig.1.2).

Comparison to simple impulse approximation predictions, including FSI, shows that the shape of the cross-sections is perfectly understood, see Figure 1.2, while the theory needs to be rescaled by 60 to 70% in order to reproduce the data. This has been attributed to correlations and other effects not present in the mean field calculation. Nonrelativistic analysis tends to derive slightly smaller spectroscopic factors, which is due to the different absorptive content of the FSI present in both approaches [16].

A complementary measurement at the larger Q^2 attainable at JLab is lacking. Such a measurement can surely shed light on the issue of the momentum dependence of the measured spectroscopic factors. Furthermore, by extending the measured region to higher missing momentum, issues such as the role of correlations as seen in low excitation energy $(e, e'p)$ results can be addressed.

A controversial issue over the last decades, has been the role of relativity in the description of nuclei. While it is true that bulk properties and many

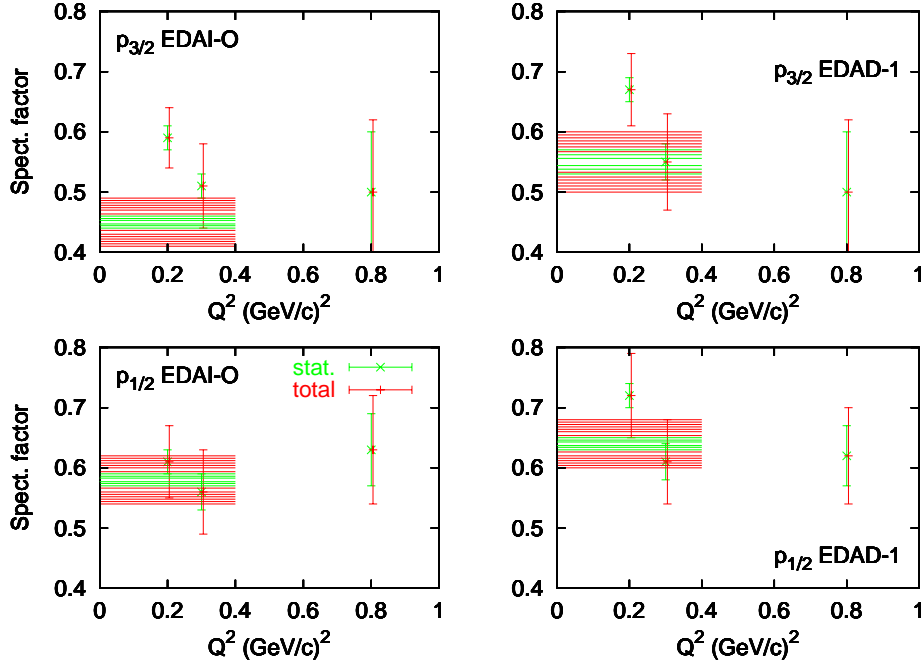


Figure 1.1: Spectroscopic factors for p-shells determined from several $^{16}\text{O}(e, e'p)^{15}\text{N}$ experiments at Saclay [10], NIKHEF [11], [12] and JLab[4]. The green and pink bands are the statistical and total errors from the parallel kinematics data set [12]. The points with the error bars were measured at fixed values of Q^2 with the same color coding as the bands. The terms EDAI-O and EDAD-1 refer to different optical model sets used in [9].

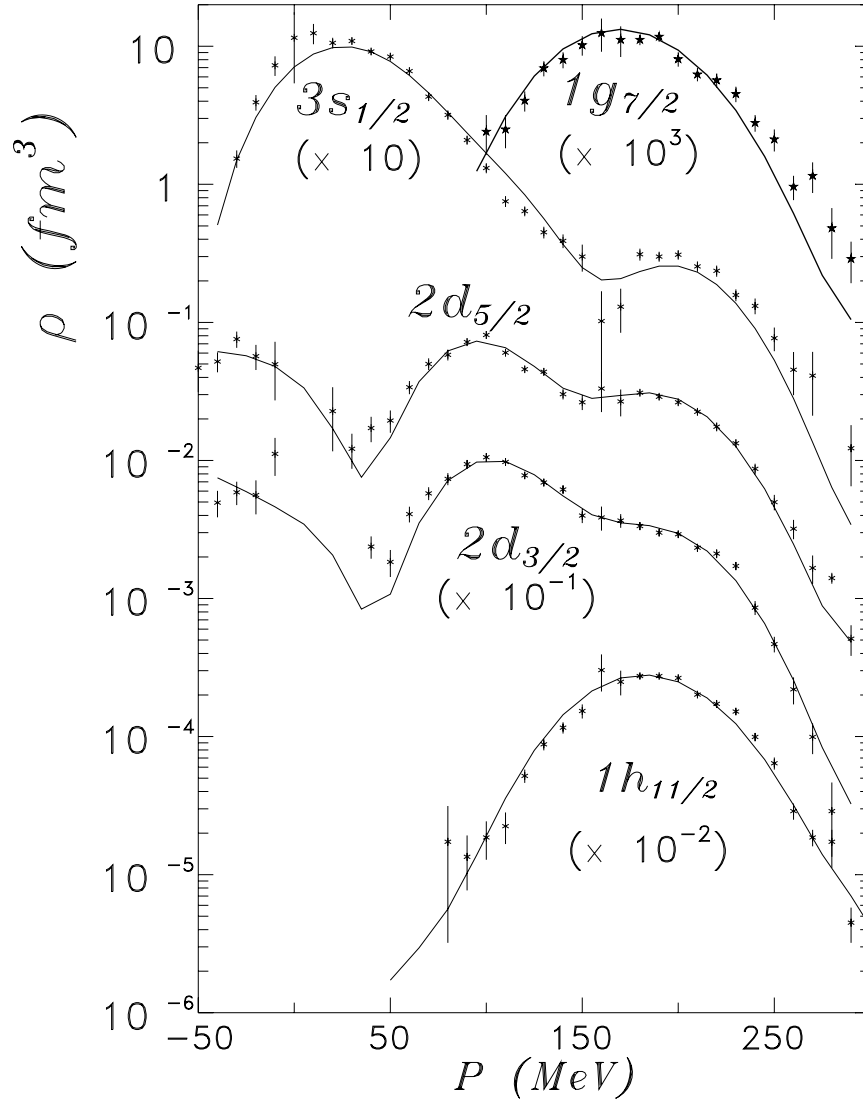


Figure 1.2: Reduced cross-sections for the outermost shells measured in $^{208}\text{Pb}(e, e'p)^{207}\text{Tl}$ experiments at NIKHEF [13] compared to predictions of the relativistic distorted wave impulse approximation (RDWIA) [15]

single-particle properties are usually well described within the standard non-relativistic formalism, there is yet the open question of whether there are any visible effects of relativity, beyond the well-known need to include spin-orbit interactions, even at the mean field level. As has been mentioned earlier, nonrelativistic analysis of $(e, e'p)$ data tends to produce larger cross-sections and thus, smaller spectroscopic factors are extracted from the same data, than relativistic analysis. This can be traced back to a known relativistic effect, the Darwin term in the nonrelativistic terminology, that causes a depletion of the density of the outgoing proton when FSI are described in the relativistic formalism based upon the Dirac equation instead of the nonrelativistic one, even if both formalism yield the same description of elastic proton scattering[17, 16].

Within the mean field, the identification of relativistic effects from the analysis of cross-sections is masked to some extent by the fact that there is one free parameter in the approach, the spectroscopic factor. So that, the cross-sections at moderate values of p_{miss} are very similar in both the relativistic and nonrelativistic impulse approximation analysis of $(e, e'p)$ data, once the spectroscopic factor has been fitted to the data. However, it has been well know for several years [18] that the relativistic calculations in constant (\mathbf{q}, ω) kinematics exhibited a larger asymmetry with respect to both sides of \mathbf{q} compared to the nonrelativistic calculations. Furthermore, at large missing momentum and for the kinematics of the NIKHEF experiment [5], the predictions of the relativistic impulse approximation for the cross-section forward of \mathbf{q} , differ much more from the ones of the nonrelativistic ones than do the cross-sections backward of \mathbf{q} . It was in this latter configuration where the proton was detected backward of \mathbf{q} that NIKHEF made its measurements. This is illustrated in Figure 1.3 for the transition to the ground state of ^{207}Tl . This enhancement of the left-right asymmetry of the cross-section is due to the enhancement of the R_{TL} response due to dynamical relativistic effects, namely the enhancement of the lower components of the spinors [19, 20].

The spectroscopic factor ambiguity, as well as many systematic errors, can be removed if one focusses on an observable that is a ratio of cross-sections. So that, the A_{TL} asymmetry, or ratio between the difference of the cross-sections at both sides of \mathbf{q} divided by the sum, that is proportional to the TL contribution to the cross-section, has been proposed [4] to assess the departure of the $(e, e'p)$ data from the expected single photon approximation behaviour. As well as being free from spectroscopic factor ambiguities,

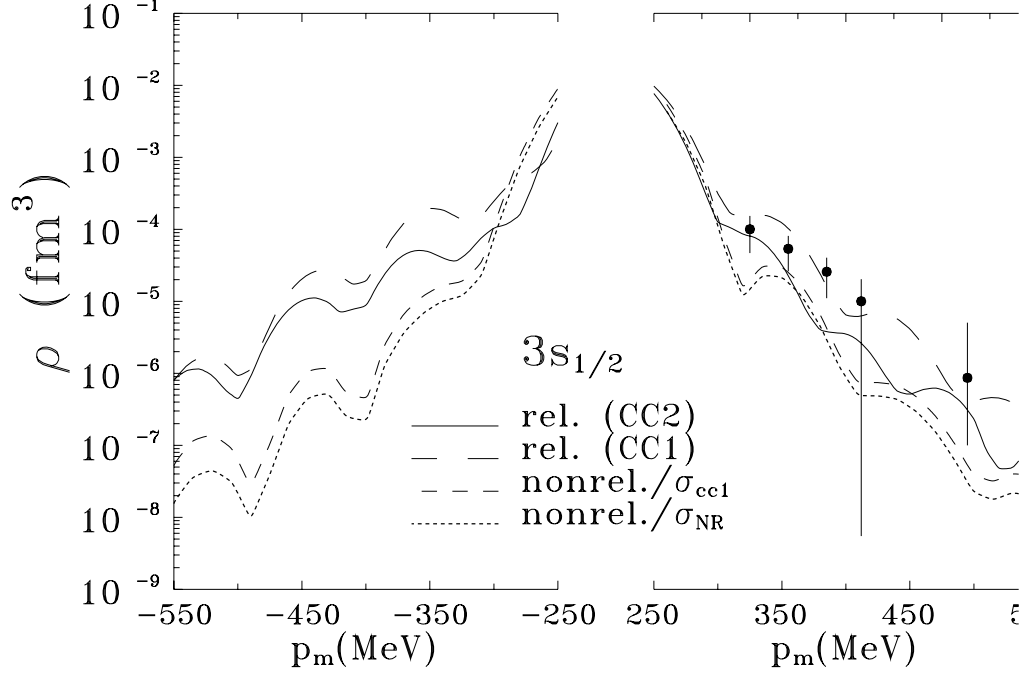


Figure 1.3: Reduced cross-sections for the $3s_{1/2}$ shell measured in $^{208}\text{Pb}(e, e'p)^{207}\text{Tl}$ experiments at NIKHEF at high [5] missing momentum compared to predictions of the relativistic distorted wave impulse approximation (RDWIA) [16]. The relativistic and nonrelativistic predictions are also shown. Notice that on the side of q measured at NIKHEF, the difference between the two formalism is large, but long range correlations in the nonrelativistic case can produce a similar enhancement of the reduced cross-section. On the other side of q , never measured so far, however, the differences between relativistic and nonrelativistic predictions reaches up to two orders of magnitude, which will not be explained by long range correlations alone.

the A_{TL} ratio would immediately reveal departure of the data from the free, factorized behavior [21]. This observable has been found extremely sensitive to relativistic effects at intermediate missing momentum ($p_{miss} < 300$ MeV/c), while FSI, MEC and other effects can also influence this observable for $p_{miss} > 300$ MeV/c ([22] and Fig.2.3).

The goals of this proposal are to measure with good statistics the reduced cross-sections for the outermost shells of ^{208}Pb , at the same kinematics of the two experiments already performed in ^{16}O at JLab, that is, in quasielastic kinematics with (\mathbf{q}, ω) constant, transferred q of 1 GeV/c and up to missing momentum well in excess of 400 MeV/c. The A_{TL} asymmetry will also be determined with high accuracy at the widest possible p_{miss} range. The high missing energy region will also be simultaneously explored.

1.2 Physics Motivation

Measurement of $(e, e'p)$ cross-sections at large missing momentum can reveal information on the high momentum distributions of nucleons in nuclei which, in turn, can be due to correlations, FSI, relativistic effects or MEC effects. While the enhancement of the high momentum components of the nucleon inside nuclei due to short range correlations is expected to be small for states at low excitations energies [23], it has been claimed that long range correlations produce a large excess of momentum distribution at high missing momentum [24]. Excess of strength at high missing momentum compared to a mean field nonrelativistic impulse approximation calculation was found in [5] and the issue of the role of long range correlations versus relativistic effects has been raised but not completely settled yet.

One particular point makes the analyses of the measurement at NIKHEF complicated, namely the kinematics chosen was not near $x_B = 1$. This was due to the limited electron beam energy and conversely modest momentum transfer. So that, in order to achieve large missing momentum with these constraints, values of x_B rather far from the quasielastic peak were chosen in constant (\mathbf{q}, ω) kinematics. In Figure 1.4 the results for both the low- p_{miss} experiments of Quint, in parallel kinematics, and the ones at high- p_{miss} are displayed, along with a few theoretical predictions. From these measurements, excess strength compared to the standard mean field calculations was found. This strength was explained via correlations in a nonrelativistic formalism, but also by relativistic effects in the mean field model [16] and

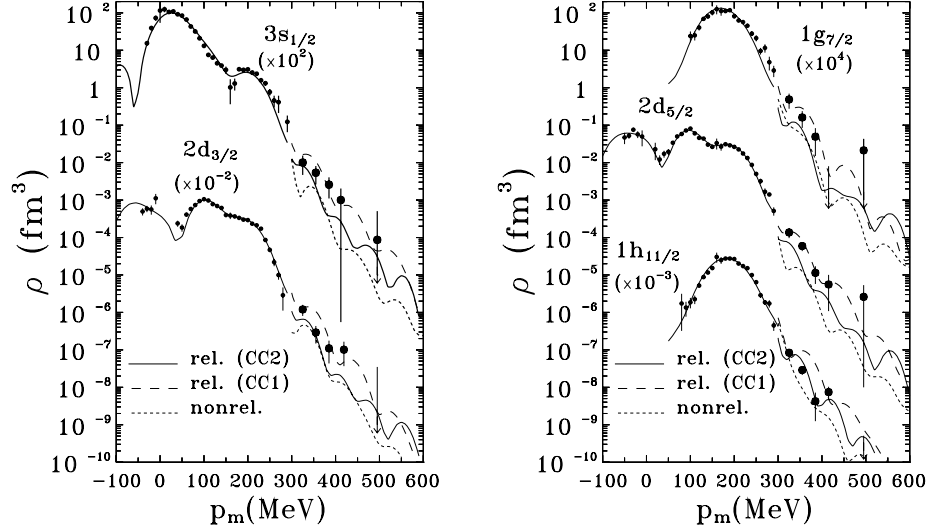


Figure 1.4: Reduced cross-sections for the outermost shells measured in $^{208}\text{Pb}(e, e'p)^{207}\text{Tl}$ experiments at NIKHEF showing both low [13] and high [5] missing momentum regions, compared to predictions of the relativistic distorted wave impulse approximation (RDWIA) obtained with the *cc1* and *cc2* current operators, and with an equivalent nonrelativistic calculation [16]

Figure 1.4.

It is important to verify that excess strength is indeed also present at true quasielastic kinematics, where the same experiment with constant momentum and energy transfer can cover the whole range of missing momentum from low to high p_{miss} , and with good statistics.

1.3 Choice of Lead as a Target

There are many characteristics of the chosen target, lead, that make it the ideal candidate to pursue the goals proposed, namely, to look for additional strength at large missing momentum and to try to confirm (or to overrule) a possible dependence on Q^2 of the spectroscopic factors derived from the $(e, e'p)$ reactions.

On one hand, ^{208}Pb has been explored experimentally several times in the past, and accurate values of the spectroscopic factors were derived [13, 14, 5,

15] at Q^2 below 0.5 (GeV/c)^2 . On the other hand, this nucleus is a textbook case for the mean field models. It is doubly magic, the extreme shell model predicts accurately many of its experimentally observed features and it is large enough so that surface effects should not be dominant. Furthermore, the outermost shells (in energy), *i.e.* the ones probed under exclusive conditions, have very different angular momentum (from 0 to 5) and they sample different regions of the nuclear interior. There is one peaked in the interior, the $3s_{1/2}$ shell, and also a surface peaked one, the $1h_{11/2}$ shell. Thus a variety of medium densities would be, effectively, put in play by studying the 'exclusive' shells.

In addition, in a nucleus like this one, where many shells contribute to final state interactions, the optical model approach, either phenomenological [17] or based upon the folding and local density approaches, is very reliable. Many elastic data are available for this target and the uncertainty due to the $A - 1$ nucleons in the final state in $(e, e'p)$ compared to the A ones in the $p - A$ elastic scattering employed to fit the optical potential is much less worrisome than, for instance, for ^{16}O . Choosing a constant (\mathbf{q}, ω) kinematics similar to the one in previous JLab ^{16}O experiments [1, 25] allows both comparison with another target with fewer nucleons and also simplifies the treatment of FSI effects compared to a parallel kinematics choice. A further point that makes large A nuclei very convenient from the theoretical point of view is the fact that the contribution from MEC should not be important at high Q^2 and large A , that is, ^{208}Pb at JLab kinematics is a well suited target to avoid MEC uncertainties that, anyway, were found to be small for ^{16}O at the similar kinematics proposed here [26, 27].

Another attractive feature of heavy nuclei is the smaller Center of mass correction of the $\langle A - 1 | A \rangle$ overlap. It will not be an issue for this heavy target, compared to ^{16}O and lighter nuclei. In short, mean field calculations are sound and perfectly well established for this heavy, doubly magic nucleus and the impulse approximation approximations reaches its maximum level of predictive power under these circumstances.

Even though some Coulomb distortion of the electron wave function is expected for this heavy target, for quasielastic scattering at the electron energies proposed in this work, the effect on the cross-sections is very small and furthermore it can be exactly incorporated into the theoretical predictions [15]. The effect on A_{TL} is also small if values of the momentum at both sides of \mathbf{q} that take into account the shift in effective missing momentum due to the Coulomb distortion of the electron are used. The theoretical cross-

sections and A_{TL} asymmetry displayed in this proposal take into account the Coulomb distortion of the electron.

Thus the theoretical framework is much better determined for ^{208}Pb than for $A < 16$ targets. Yet, there are no (\mathbf{q}, ω) constant experimental studies of $(e, e'p)$ reactions for lead (on both sides of \mathbf{q} or with x_B near 1), nor has a determination of R_{TL} or A_{TL} ever been attempted.

1.4 Chasing Correlations

It has been realized for a while now that looking for unmistakable signatures of correlations from exclusive $(e, e'p)$ cross sections alone is a hard task. It is true that they are important in order to explain the cross-sections for light systems (see [28] and Figure 2.1) but, for complex nuclei, disentangling correlations from FSI, MEC and relativistic effects is very difficult. According to the nonrelativistic results in ref. [5], long range correlations were held responsible for the extra strength seen at large p_{miss} compared to the mean field approximation.

Correlations, on the other hand, will not in general introduce extra TL strength at moderate p_{miss} , and thus A_{TL} is hardly influenced by them. Long range correlations and surface effects should show a strong shell-dependence for ^{208}Pb . A_{TL} and R_{TL} however, do display differences in the approach employed being relativistic or not.

If correlations were the reason for the extra strength found in [5] at high p_{miss} , then we do not expect a particularly large effect on TL observables. On the other hand, if relativistic dynamical effects are the main cause responsible for the extra strength, a strong effect on A_{TL} , much more important than the one seen in ^{16}O (actually around twice as large) would be seen.

The measurement proposed in this work would provide the opportunity of mapping out the A -dependence of the TL observables, due to the variations in the nuclear density. In order to achieve this, a comparison of JLab high quality data for $^3,^4\text{He}$, ^{16}O and ^{208}Pb , with accuracy and unprecedented level of detail for $p_{miss} < 300$ MeV/ c as well as with the highest p_{miss} ever reached will be vital. Thus, the measurements for lead would complement recent $(e, e'p)$ experiments.

All together, the information provided by these experiments would constitute an unique test of the relativistic prediction for the A_{TL} enhancement and the nuclear density dependence that such enhancement exhibits due to

relativistic dynamical effects. For instance, very little or no additional TL-enhancement is predicted for ^3He [28], there is a visible effect in the case of ^{16}O and a very noticeable, unmistakable enhancement for a heavy nucleus like lead is predicted.

Additionally, if the shape of the momentum distribution is obtained with high precision, it would constitute the most stringent test ever of the mean field approach to $(e, e'p) < A - 1 | A >$ overlaps. Details of the bound state wave function, such as radii, would be derived with high accuracy.

In summary for the physics motivation: The experiment proposed would determine the spectroscopic factors with high reliability from good statistics data in the moderate p_{miss} region. Comparison with past experiments and with the predictions with and without long range correlations would confirm (or cast in doubt) the interpretation of the results of [5].

This measurement provides the data to determine the importance of dynamical relativistic effects in the nuclear medium predicted by the relativistic mean field model. This one all encompassing simple model determines the A_{TL} observable, which depends on the enhancement of the lower component of the wave function, the spectroscopic factors responsible for the cross section in the moderate p_{miss} region, and the strength of the cross sections at large p_{miss} .

Chapter 2

Relation to other JLab Proposals

Part of the present proposal was already presented in PR89-046. That proposal included ^{208}Pb along with two other closed shell nuclei in an investigation of the cross section as a function of p_{miss} and a longitudinal/transverse separation. All the measurements were proposed to be done in parallel or anti-parallel kinematics. The lead target was to be the focus for 420 hours of requested beam time at $30\text{ }\mu\text{A}$ at 2 GeV and 4 GeV beam energy. The principle experimental issues addressed in that proposal dealt with the 350 keV or better resolution needed to separate final states.

PAC4 approved this proposal conditionally with the stipulation that the experimenters could demonstrate separating levels spaced as closely as 350 keV with relative strengths differing by a factor of ten. We did realistic GEANT simulations for our kinematics using the known properties of the Hall A spectrometers. The results for the resolution study are in Table 2.1. The targets listed in this table are discussed in Appendix B. From this we conclude that the minimum FWHM intrinsic resolution of the missing mass spectrum for the proposed studies is about 0.5 MeV due to the spectrometers alone.

We believe we can address the issue of extracting the desired information despite the larger than desired FWHM in two ways: Chapter 4 discusses analyzing the spectrum in groups of three well separated regions containing, at least for the first 2.5 MeV of excitation energy only groups of two unresolved states. Appendix B discusses fitting the spectra with realistic line profiles to extract the individual peaks.

target	thickness	spectrometer	dE total
	mm		MeV
C/Pb/C	0.2	realistic	0.88
C/Pb/C	0.2	ideal	0.706
C/Pb/C	0.1	realistic	0.66
NIKHEF-target	2 x 0.038	realistic	0.66
NIKHEF-target	1 x 0.038	realistic	0.52
NIKHEF-target	1 x 0.038	ideal	0.2
NIKHEF-paper	1 x 0.038		0.18

Table 2.1: A comparison of the resolution for various target configurations, excluding the radiative tail. The realistic spectrometer settings use the published Hall A spectrometer characteristics [29]. The ideal spectrometer settings contribute no width. NIKHEF-target refers to using the NIKHEF two foil or one foil targets in our spectrometers and kinematics. NIKHEF-paper refers to the results from [5]. In that experiment the scattered electron energy was almost 7 times lower than in the proposed kinematics. A comparison of the widths for the same target between the realistic and ideal spectrometers gives us a measure of the spectrometers' contribution to the experimental FWHM. Assuming the target effects and spectrometer effects add in quadrature we conclude that the spectrometers contribute about 0.5 MeV to the FWHM for our kinematics.

Previous $(e, e'p)$ experiments on ^3He and ^{16}O at Jefferson lab and approved experiment E04-107 on ^4He for which the lead data would provide a useful comparison are shown in Figures 2.1, 2.2 and 2.3. Chapter 1.4 discussed the A dependence and density dependence expected for A_{TL} .

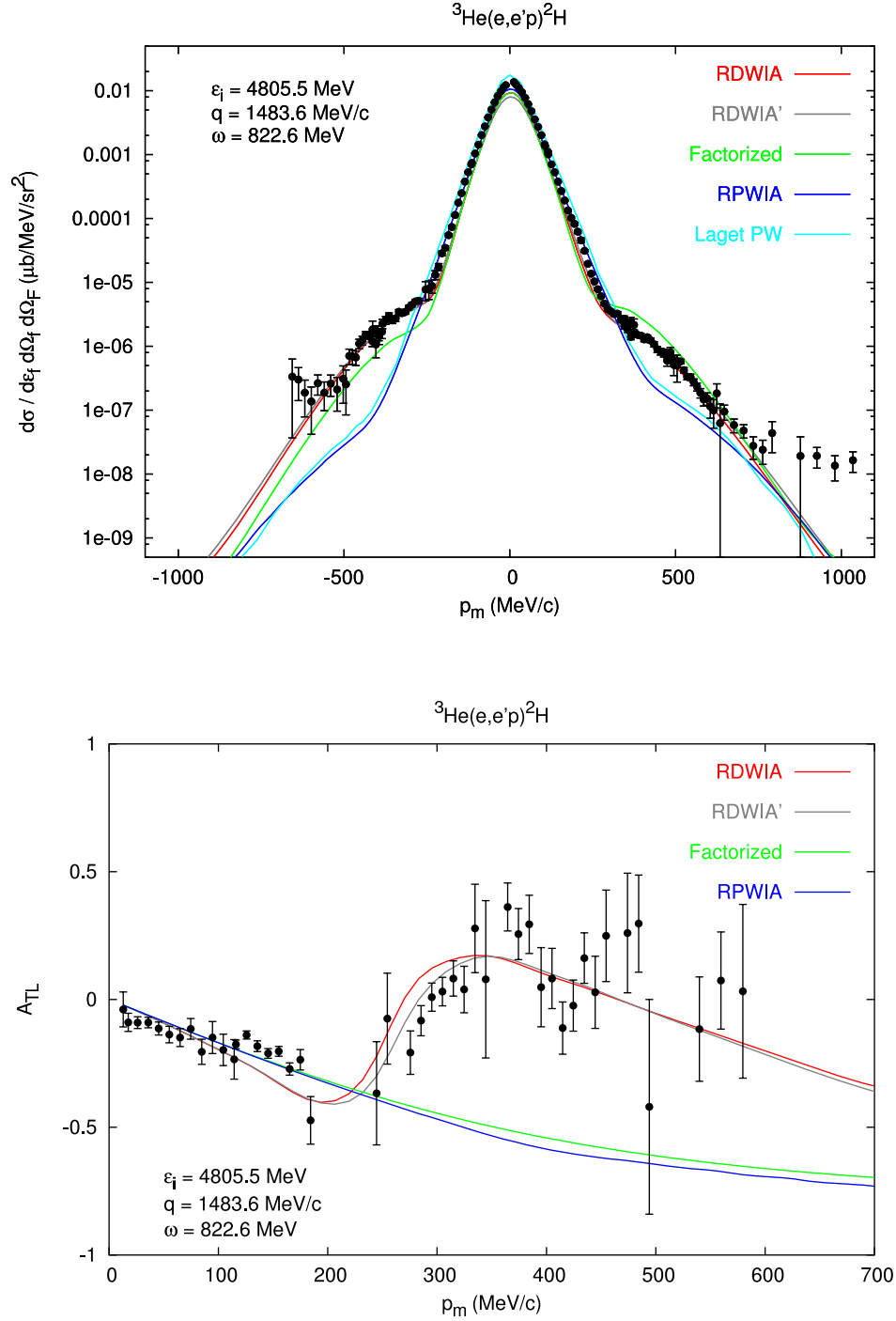


Figure 2.1: Cross-sections for the ${}^3\text{He}(e,e'p){}^2\text{H}$ experiment at high Q^2 [30] compared to predictions of the relativistic distorted wave impulse approximation (RDWIA) with realistic overlaps from relativized Faddeev calculations with AV8 interaction (RDWIA), standard nonrelativistic Faddeev (RDWIA) and PWIA and factorized results. The A_{TL} asymmetry is shown in the lower figure. Correlations are fundamental to explain the cross-section, while relativistic effects affect A_{TL} just a little [28].

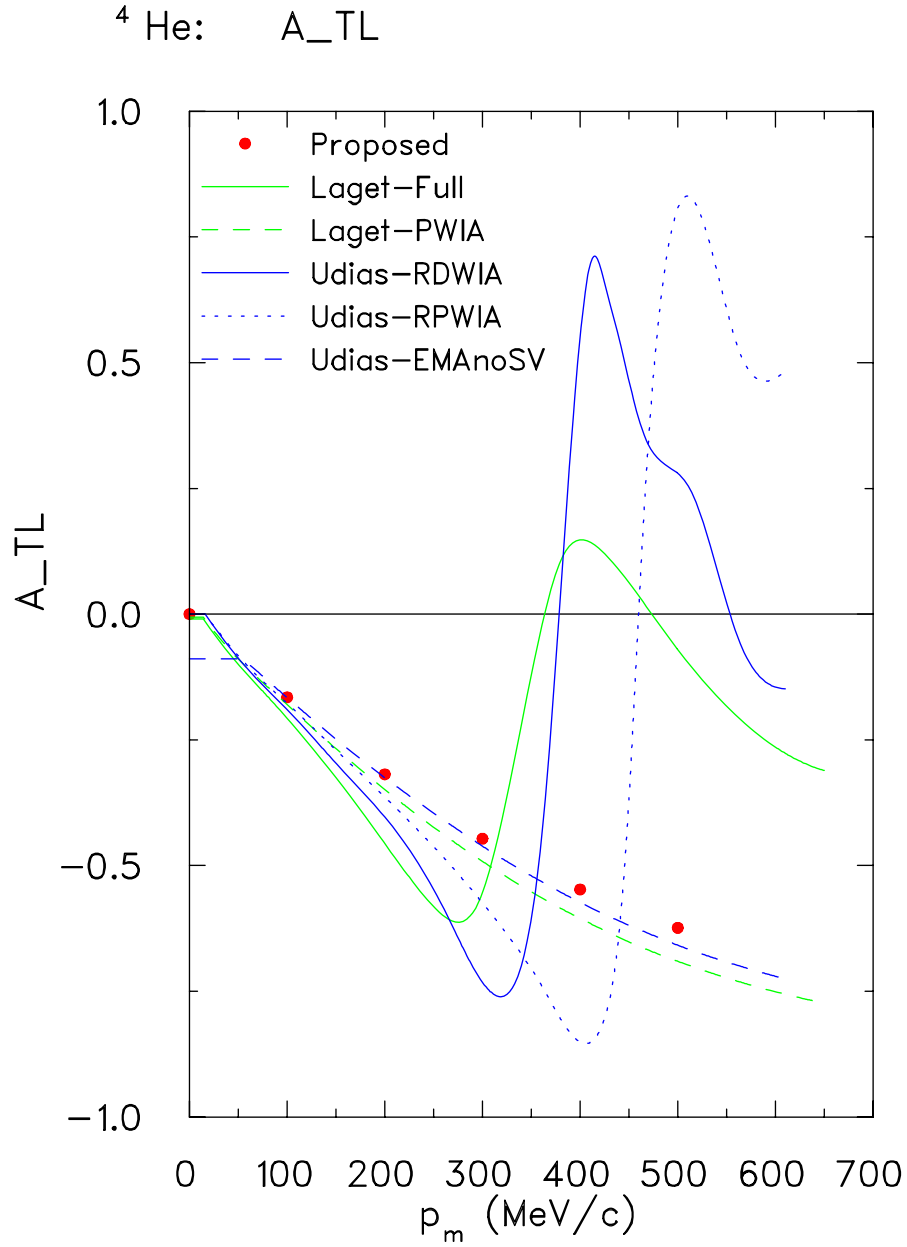


Figure 2.2: A_{TL} predicted for the $^4\text{He}(e, e'p)^3\text{H}$ reaction from [31]. A stronger amplitude in A_{TL} here in ^4He than in ^3He is attributed to the greater density of the heavier nucleus.

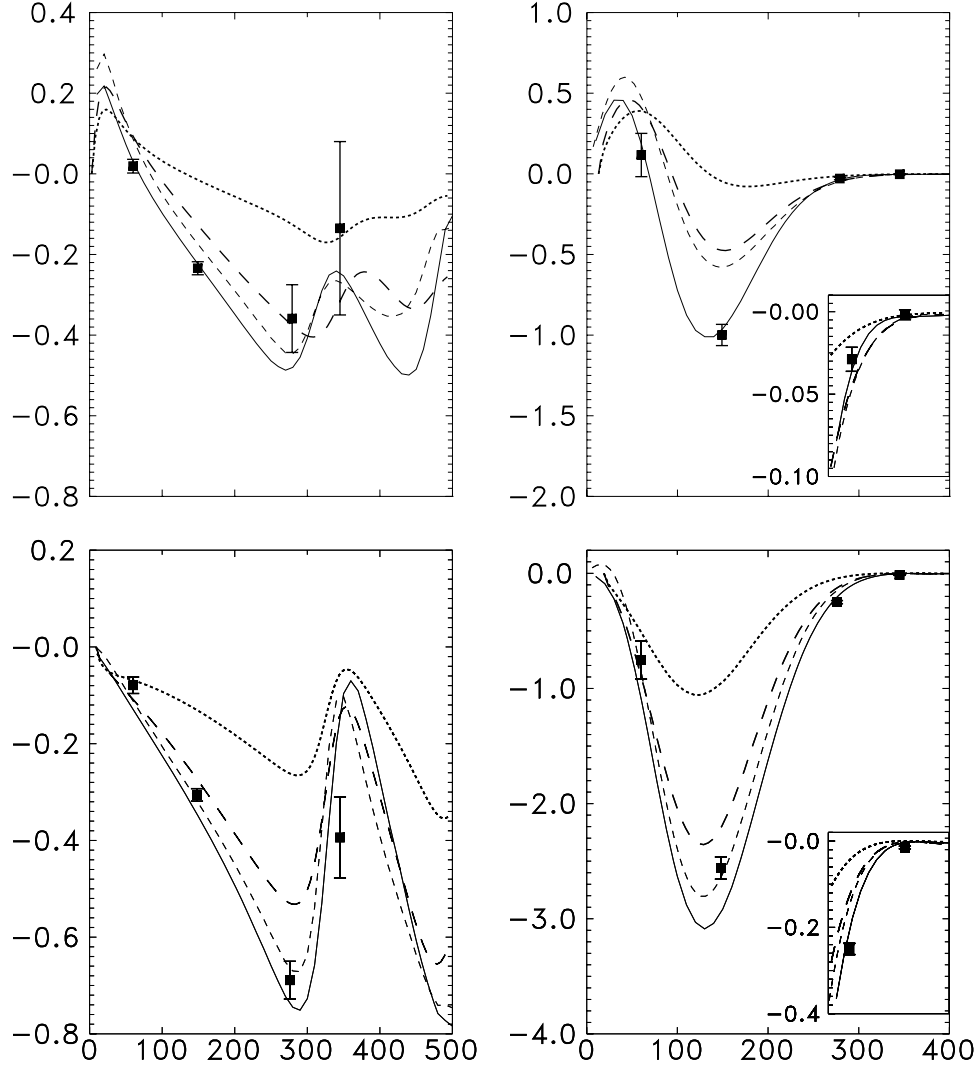


Figure 2.3: A_{TL} (left) and R_{TL} response (right) measured in $^{16}\text{O}(e, e'p)^{15}\text{N}$ experiments at JLab [4] compared to predictions of the fully relativistic distorted wave impulse approximation (RDWIA) [22] given by solid lines, and calculations where the enhancement of the lower components of the spinors in the relativistic calculation is not taken into account (short dashed, with the full operator, and long dashed, with a relativized nonrelativistic current operator). Dotted line represents the results obtained with a typical nonrelativistic current operator). Above, $p_{1/2}$ shell. Below, $p_{3/2}$ shell.

Chapter 3

Theoretical Predictions

Due to resolution requirements, it is likely that we cannot resolve some states. With proper kinematical cuts, contributions from at least three distinct regions in the exclusive ($E_m < 16$ MeV) region will be isolated:

1) Region 1, missing energy from 0 (g.s.) to 1. MeV above g.s.(ground state). This would include g.s. $3s_{1/2}$ knock-out as well as the $2d_{3/2}$ shell knock-out as dominant contributors. Results added with the right weights for this region are presented in Figure 3.1

For these shells with relatively low angular momenta, the maximum of the cross-section appears at relatively low missing momentum. At missing momentum of 100 MeV/ c , where the cross-section peaks it should be possible to obtain very small error bars. The predictions for A_{TL} from the full relativistic formalism are clearly different from the ones of the 'projected' approach, representing the prediction from standard 'nonrelativistic' models of nuclear structure, where only dispersive as well as spin-orbit effects break factorization. For comparison, results of a calculation that only includes spin-orbit distortion of the spinors via FSI, are also shown. Note that due to the different p_{miss} behaviour of the s and d contributions (they peak at very different values of p_{miss}), provided high statistics is achieved for $p_{miss} < 350$ MeV/ c , the values of the spectroscopic factors for the separated s and d contributions would be reliably extracted.

2) Region 2, missing energy from 1 to 2.5 MeV. above g.s.. This region would mostly get contributions from knock-out from $1h_{11/2}$ and $2d_{5/2}$ shells. The two distinct peaks from the d and h shells are clearly seen in Fig. 3.2.

Maxima of the cross-section in this case lies at slightly larger value of missing momentum, approximately 200 MeV/ c . As in the previous case, it is

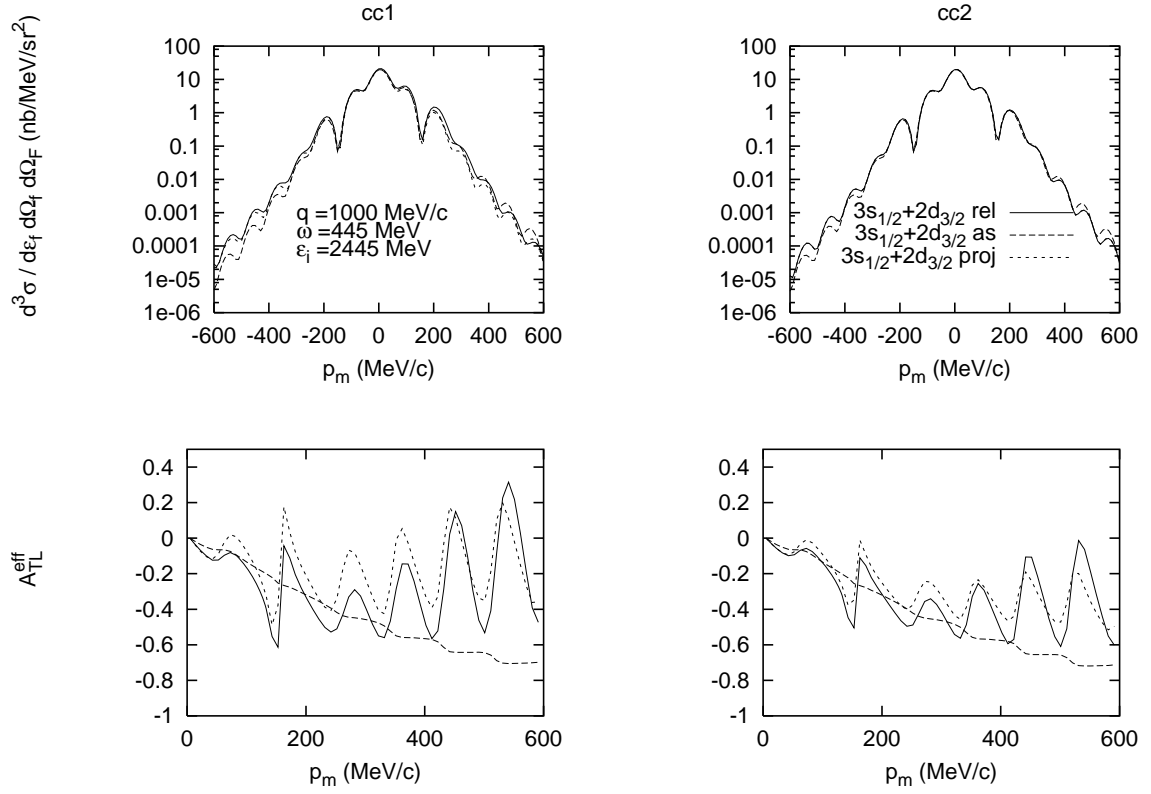


Figure 3.1: Predicted cross sections and A_{TL} for the summed transitions to the ground state ($3s_{1/2}$) and 0.351 MeV state ($2d_{3/2}$) for $^{208}\text{Pb}(e, e'p)^{207}\text{Tl}$.

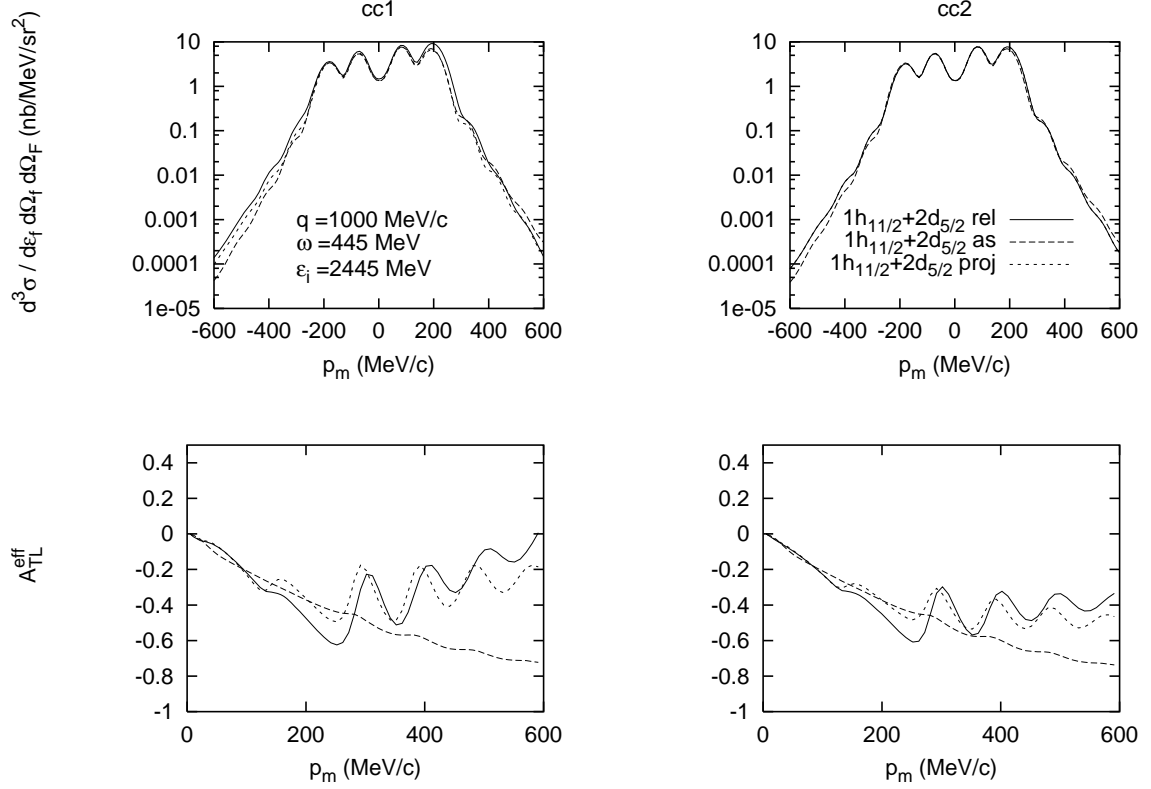


Figure 3.2: Predicted cross sections and A_{TL} for the summed transitions to the 1.348 MeV state ($1h_{11/2}$) and 1.683 MeV state ($2d_{5/2}$) for $^{208}\text{Pb}(e, e'p)^{207}\text{Tl}$.

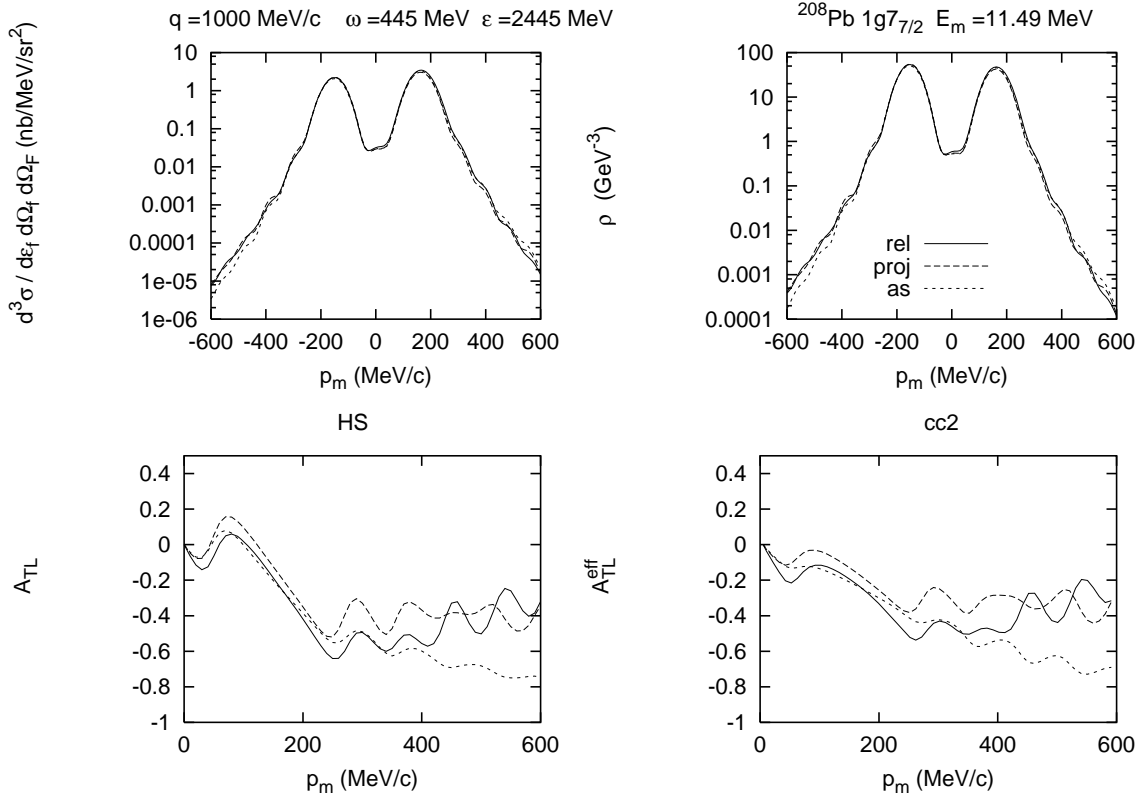


Figure 3.3: Predicted cross sections and A_{TL} for the transitions to the $1g_{7/2}$ shell at 3.470 MeV for $^{208}\text{Pb}(e, e'p)^{207}\text{Tl}$.

precisely for this value of missing momentum where A_{TL} shows the highest sensitivity to the modification of the structure of the spinors due to the relativistic mean field. Actually, the first peak at both sides of \mathbf{q} received no contribution from the $1h_{11/2}$ shell and thus an almost model independent extraction of the scale factors for each shell should be here very easy.

3) Region 3, missing energy from 2.5 to 5 MeV above g.s. This region would receive contribution from knock-out from the $1g_{7/2}$ shell. Again, relativistic predictions deviate clearly from projected ones precisely where the count rate should be more favourable. This can be seen in Fig. 3.3.

DEEP MISSING ENERGY

Contrary to the case of light nuclei like ^{12}C or ^{16}O where at energy transfer beyond exclusive conditions, that is, where the missing energy is enough to allow for more complex processes than just knocking out a single nucleon,

only a couple of nucleons from $1s_{1/2}$ contribute, the 'direct' single nucleon knockout is the result of a sum over many different shells and many nucleons can contribute here. Thus, at energies well below pion threshold and that lie in the dip, before the delta propagation inside the nucleus should show up, the contribution of direct single nucleon knock-out should constitute a very important fraction of the strength measured at $12 \text{ MeV} < E_m < 80 \text{ MeV}$ and so it has been found in a recent experiment at NIKHEF [14]. This is in contrast to what has been observed in ^{12}C and ^{16}O where the contribution of the impulse approximation model in this region is important only at low missing momentum. A comparison of the data for ^{208}Pb alongside with the ones for ^{16}O would shed light on the role played by IA, MEC and IC contributions to this high missing energy region.

Chapter 4

Kinematics and Experimental Rates

4.1 Experimental Setup

Hall A has proven itself capable of extracting high quality response functions [4, 27]. In fact, these results from the reaction $^{16}\text{O}(e, e'p)$ came from the first experiment to be performed in Hall A and since then the knowledge of the spectrometers has been continually improving. Presently, the analysis of the $^3\text{He}(e, e'p)$ and $^2\text{H}(e, e'p)$ experiments are complete and there is an approved Hall A experiment (E04-107) to measure accurate cross sections and extract the response functions from the $^4\text{H}(e, e'p)$ reaction.

We plan to measure the reaction $(e, e'p)$ in ^{208}Pb , by making use of the techniques developed from these experiments and the Hall A high resolution spectrometers. With a missing energy resolution of 1 MeV, the two-body peak, located at 8 MeV, will be well separated from the $^{12}\text{C}(e, e'p)^{11}\text{B}$ g.s. which begins at 16 MeV for the diamond/lead sandwich target described below.

Cross sections, count rate calculations, and simulations for the proposed measurements were estimated using a beam current of 100 μA on a 0.2 mm thick ^{208}Pb target sandwiched between two 0.15 mm sheets of diamond, which is pure ^{12}C . This translates to a target luminosity of $5 \times 10^{35} \text{ cm}^{-2} \text{ sec}^{-1}$.

The standard properties of the Hall A spectrometers were used in making the count rate estimates: solid angles of 5 msr and momentum bites of $\pm 4.5\%$. We used a spectral function $S(p_m)$ (Figure 4.1) for the $3s_{1/2}$ g.s. which

we obtained from J.Udias [32]

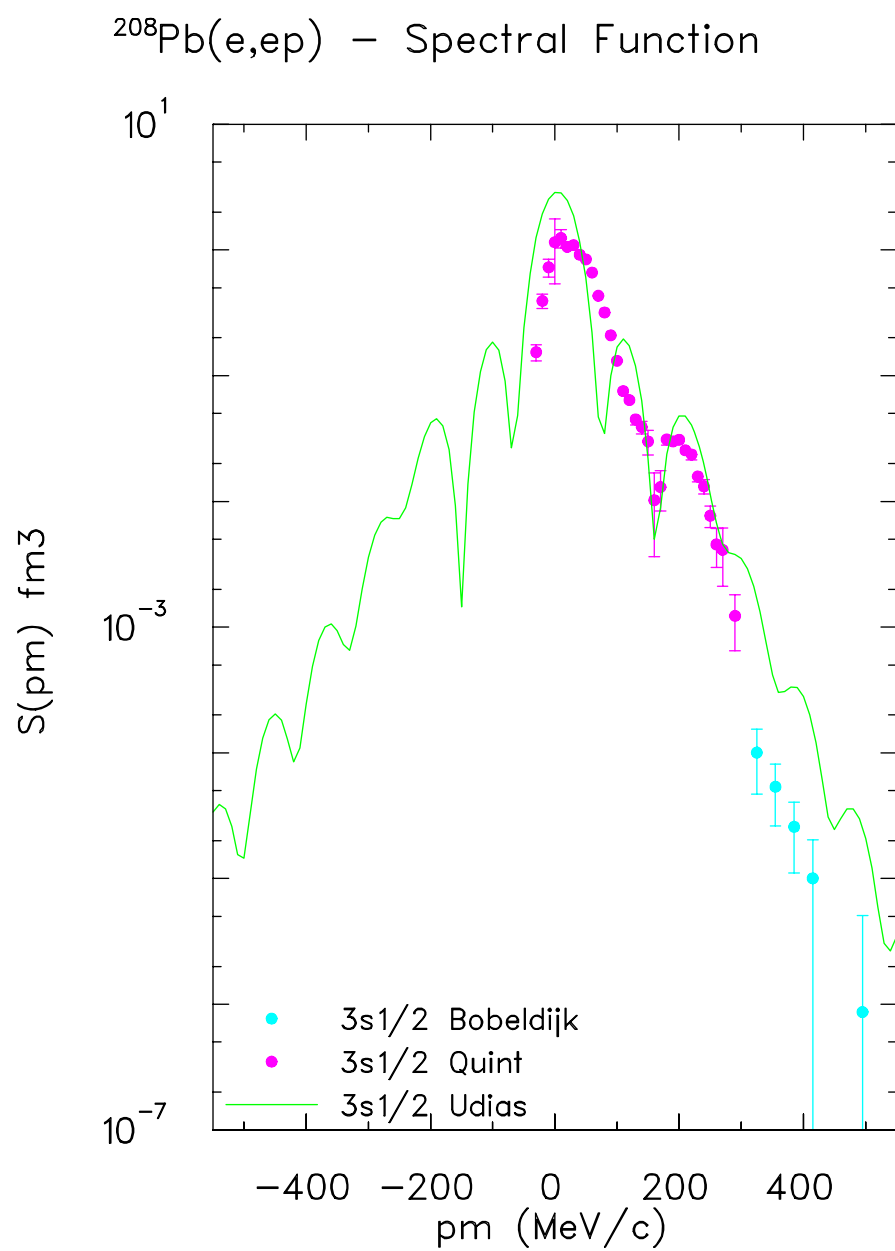


Figure 4.1: Shown above is the parameterization of the ^{208}Pb spectral function from J. Udias and experimental results from NIKEF [5], [13]

4.2 Proposed Kinematics

In the perpendicular kinematics, shown in Table 4.1, q will be fixed to 1.0 GeV/ c and ω will be fixed to 0.433 GeV. With this constraint, the $(e, e'p)$ cross section will be measured with a beam energy of 2.445 GeV with protons detected on either side of the q -vector. This will allow the extraction of the A_{TL} asymmetry.

Table 4.1: Perpendicular Kinematics

Kinematics	\mathbf{q} [GeV/ c]	E_o [GeV]	ω [GeV]	ϵ	E_e [GeV]	θ_e [degrees]	P_p [GeV]	θ_p [degrees]	p_m [GeV/ c]
Kin01	1.0	2.445	0.433	0.904	2.012	23.45	0.99	53.19	0.000
Kin02	1.0	2.445	0.433	0.904	2.012	23.45	0.99	58.92	0.100
Kin03	1.0	2.445	0.433	0.904	2.012	23.45	0.99	47.46	0.100
Kin04	1.0	2.445	0.433	0.904	2.012	23.45	0.99	64.72	0.200
Kin05	1.0	2.445	0.433	0.904	2.012	23.45	0.99	41.67	0.200
Kin06	1.0	2.445	0.433	0.904	2.012	23.45	0.99	70.53	0.300
Kin07	1.0	2.445	0.433	0.904	2.012	23.45	0.99	35.85	0.300
Kin08	1.0	2.445	0.433	0.904	2.012	23.45	0.99	76.42	0.400
Kin09	1.0	2.445	0.433	0.904	2.012	23.45	0.99	29.99	0.400
Kin10	1.0	2.445	0.433	0.904	2.012	23.45	0.99	82.32	0.500
Kin11	1.0	2.445	0.433	0.904	2.012	23.45	0.99	24.07	0.500

4.3 Singles Rates

The single-arm background rates is shown for the perpendicular kinematics in Table 4.2. The (e, e') rate were calculated with the QFS computer code and the (e, p) , (e, π^+) , and (e, π^-) rates were calculated with the EPC code of Lightbody and O'Connell [33]. The rates were calculated for a luminosity of 5.0×10^{35} cm²/s. As demonstrated during the E89-003 $^{16}\text{O}(e, e'p)$ experiment, which made measurements in similar kinematics, rates such as these are not a problem for the Hall A spectrometers.

4.4 Coincidence Rates

We determined the coincidence rates by assuming a luminosity of $5 \times 10^{35} \text{ cm}^{-2} \text{ sec}^{-1}$. A missing energy width of 1.6 MeV and a timing width of 2 ns was used to determine the true and accidental rates. The computer code SEEX [34] was used in computing the fivefold differential cross sections (denoted as σ_5 in the tables) at each kinematic point.

4.5 Systematic and Statistical Uncertainties

With careful luminosity monitoring and elastic cross section measurements at appropriate energies we should be able to achieve a systematic uncertainty of 3% as exhibited in the E89-044 experiment on ^3He . We have therefore assumed a systematic uncertainty of 3% for all our cross section measurements. In Table 4.3 the uncertainty in the five-fold differential cross sections, denoted as σ_5 , includes only the statistical uncertainty. If the cross sections for kin10 and kin11 are as small as theory predicts then we will not be able to obtain sufficient counts to do the peak fitting discussed in Appendix B. However, the group near the ground state and the group near 1.5 MeV will be treated as composite peaks in the manner discussed in chapter 3. We will still be able to obtain cross sections and information about the strength in this large p_{miss} region to confront theories attempting to explain the strength. The group (0, 0.350) will have a statistical uncertainty of about 17% and the group at (1.348, 1.683) will have 10% statistical accuracy for kin10 and 30% and 12% for kin11, respectively.

Table 4.2: Singles rates for the perpendicular kinematics.

Kinematics	(e, e') KHz	(e, π^-) KHz	(e, p) KHz	(e, π^+) KHz
Kin01	5.8	7	8.4	25
Kin02	5.8	7	2	<1
Kin03	5.8	7	22.4	26
Kin04	5.8	7	1.6	<1
Kin05	5.8	7	27.1	26
Kin06	5.8	7	1.2	<1
Kin07	5.8	7	31.6	27
Kin08	5.8	7	1	<1
Kin09	5.8	7	35.6	27
Kin10	5.8	7	<1	<1
Kin11	5.8	7	39.4	28

Table 4.3: Perpendicular kinematics.

Kinematics	p_m [GeV/c]	σ_5 [b/GeV/sr ²]	Coinc. [1/hr]	Time [hr]	$\delta\sigma_5$
Kin01	0.000	0.194E-04	0.565E+05	1.0	<1%
Kin02	0.100	0.137E-05	0.397E+04	5.5	<1%
Kin03	0.100	0.105E-05	0.304E+04	4.5	<1%
Kin04	0.200	0.459E-06	0.133E+04	5.9	1%
Kin05	0.200	0.197E-06	0.573E+03	4.1	2%
Kin06	0.300	0.395E-07	0.115E+03	11.5	2.8%
Kin07	0.300	0.140E-07	0.407E+02	8.5	6.8%
Kin08	0.400	0.361E-08	0.105E+02	20.	7.3%
Kin09	0.400	0.922E-09	0.268E+01	30.	36.2%
Kin10	0.500	0.304E-09	0.882E+00	24.	22.%
Kin11	0.500	0.407E-10	0.118E+00	24.	58.%

Chapter 5

Expected Results

The method of obtaining the peak areas of the five states of interest is discussed in detail in Appendix B. The uncertainties in the areas is mainly due to extracting individual peaks using the fitting procedure. A table illustrating the expected counts and fitting errors associated with peak extractions is shown in Table 5.1.

Predicted values for the asymmetry, A_{TL} for three theoretical prescriptions are shown in Figures 5.1, 5.2, 5.3, 5.4, 5.5 along with expected uncertainties at selected values of p_{miss} .

Within the impulse approximation, we compute the $(e, e'p)$ response with an one-body electromagnetic operator. Thus, the matrix element just splits in two terms. We define the overlap of the 'spectator nucleons', that is, the ones that do not interact with the exchanged photon as follows. Let's say it is the nucleon labeled 1 that interacts with the photon. Then we have:

$$\hat{\Psi}_{IF}(\vec{p}_1) = \int d\vec{p}_2 \dots d\vec{p}_A \bar{\Psi}_F(\vec{p}_2, \dots, \vec{p}_A) \Psi_I(\vec{p}_1, \vec{p}_2, \dots, \vec{p}_A).$$

Where Ψ_I, Ψ_F are the A-particle wave functions for the initial and final nuclei. Within the extreme mean field, closure and orthogonality of the single-particle states guarantee that this overlap is just the single-particle state from the shell corresponding to the nucleon '1', let's say $\Psi_B(\vec{p}_1)$. The deviation of the overlap from the single particle state is measured by the spectroscopic factor, $S = |A|^2$, where $\hat{\Psi}_{IF}(\vec{p}_1) = A\Psi_B(\vec{p}_1)$.

Beyond mean field, the overlap is computed between two general A-particle wave functions and the resulting function $\hat{\Psi}_{IF}(\vec{p}_1)$ is no longer equiv-

100MeV/c	0	0.351	1.348	1.683	3.47
cnts1-in	24352	121667	4750	136332	22261
cnts1-fit	23352	123130	2894	137318	22006
in/fit	1.04	0.99	1.64	0.99	1.01
dcnts1-fit	930	1230	1800	1370	2200
cnts2-in	14280	66343	2412	66012	13037
cnts2-fit	13539	66877	1985	66174	12940
in/fit	1.05	0.99	1.21	0.99	1.01
dcnts2-fit	740	670	430	660	130
dAtl	0.03	0.006	0.32	0.006	0.05
_____	_____	_____	_____	_____	_____
200MeV/c	0	0.351	1.348	1.683	3.47
cnts1-in	8758	24476	241372	52733	86010
cnts1-fit	7831	25138	241240	53169	85298
in/fit	1.12	0.97	1.00	0.99	1.01
dcnts1-fit	930	670	150	530	860
cnts2-in	3019	9718	60754	13035	27914
cnts2-fit	2870	9814	60513	13293	27375
in/fit	1.05	0.99	1.00	0.98	1.02
dcnts2-fit	150	100	250	270	540
dAtl	0.05	0.01	0.001	0.007	0.008
_____	_____	_____	_____	_____	_____
300MeV/c	0	0.351	1.348	1.683	3.47
cnts1-in	1447	1842	9915	3077	1695
cnts1-fit	1083	2008	10022	2954	1475
in/fit	1.34	0.92	0.99	1.04	1.15
dcnts1-fit	365	170	110	125	220
cnts2-in	379	1264	9486	2507	994
cnts2-fit	353	1144	9245	2548	836
in/fit	1.07	1.10	1.03	0.98	1.19
dcnts2-fit	30	120	240	45	160
dAtl	0.13	0.06	0.032	0.02	0.11
_____	_____	_____	_____	_____	_____

Table 5.1: Error calculations for A_{TL} due to peak extraction.

alent to any single-particle state of any mean field nor should it be normalized to any occupation number. Projecting this overlap on the appropriate single-particle (mean field) state would yield an idea of the 'mean field' content of the correlated overlap.

The matrix element of the current for the $(e, e'p)$ reaction, $J_N^\mu(\omega, \vec{q})$, can be computed as below, where the theoretical curves in the figures have the following meaning:

The solid line labelled Rel. is the full relativistic calculation using the four spinor solutions for the bound nucleon, Ψ_B , and the outgoing free nucleon, Φ_F . These four spinors are used to calculate the nucleon current $J_N^\mu(\omega, \vec{q})$.

$$J_N^\mu(\omega, \vec{q}) = \int d\vec{p}_1 \bar{\Phi}_F(\vec{p}_1 + \vec{q}) \hat{J}_N^\mu(\omega, \vec{q}) \Psi_B(\vec{p}_1).$$

Where $\hat{J}_N^\mu(\omega, \vec{q})$ is a relativistic nucleon current operator.

The dashed line labelled Proj. is a type of nonrelativistic calculation for which the nucleon current $J_N^\mu(\omega, \mathbf{q})$ is calculated with the positive-energy projections Ψ_B^{++} and Φ_F^{++} of Ψ_B and Φ_F . In this way, the relativistic enhancement of the lower components is removed from the full nucleon current. This calculation should then have the same dynamics as a nonrelativistic calculation employing the same current operator. The dynamical enhancement of the lower components is contained in the full calculation of the nucleon current, but not in the projected calculation.

The dashed-dot line labelled 'Fact' represents an idealization where the impulse approximation matrix element breaks into two factors representing the e-p elementary amplitude times the nuclear overlap. Apart from small effects due to spin-orbit coupling in the FSI, this factorization of the amplitudes translates into a factorization of the cross-section into the e-p cross-section times the spectral function. This is discussed briefly in chapter 3 and in depth in [9].

$^{208}\text{Pb}(e,ep) \ 3s_{1/2} \ A_{TL}$

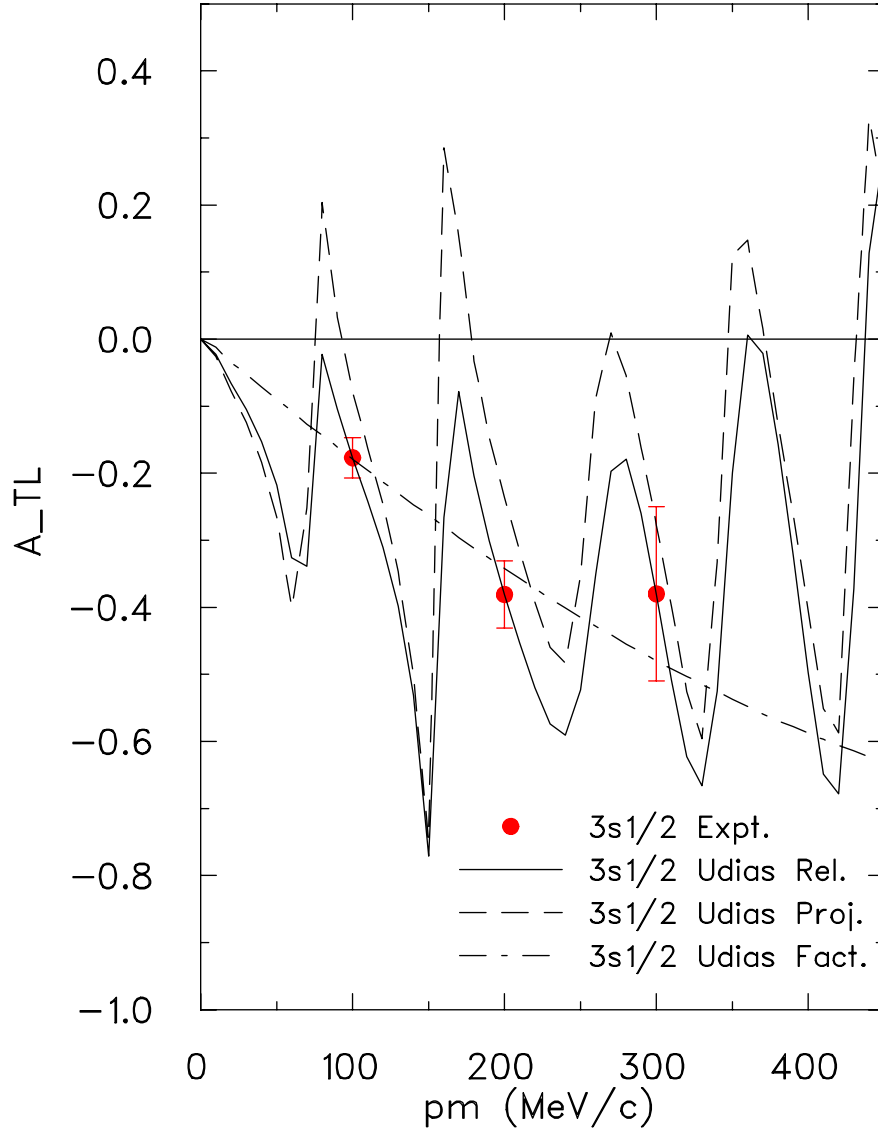


Figure 5.1: A_{TL} for the $3s_{1/2}$ ground state of ^{207}Tl . The experimental uncertainties are indicated at 100, 200 and 300 MeV/ c . The meaning of the theoretical curves is described in the text.

$^{208}\text{Pb}(e,ep) \text{ } 2d_{3/2} \text{ } A_{TL}$

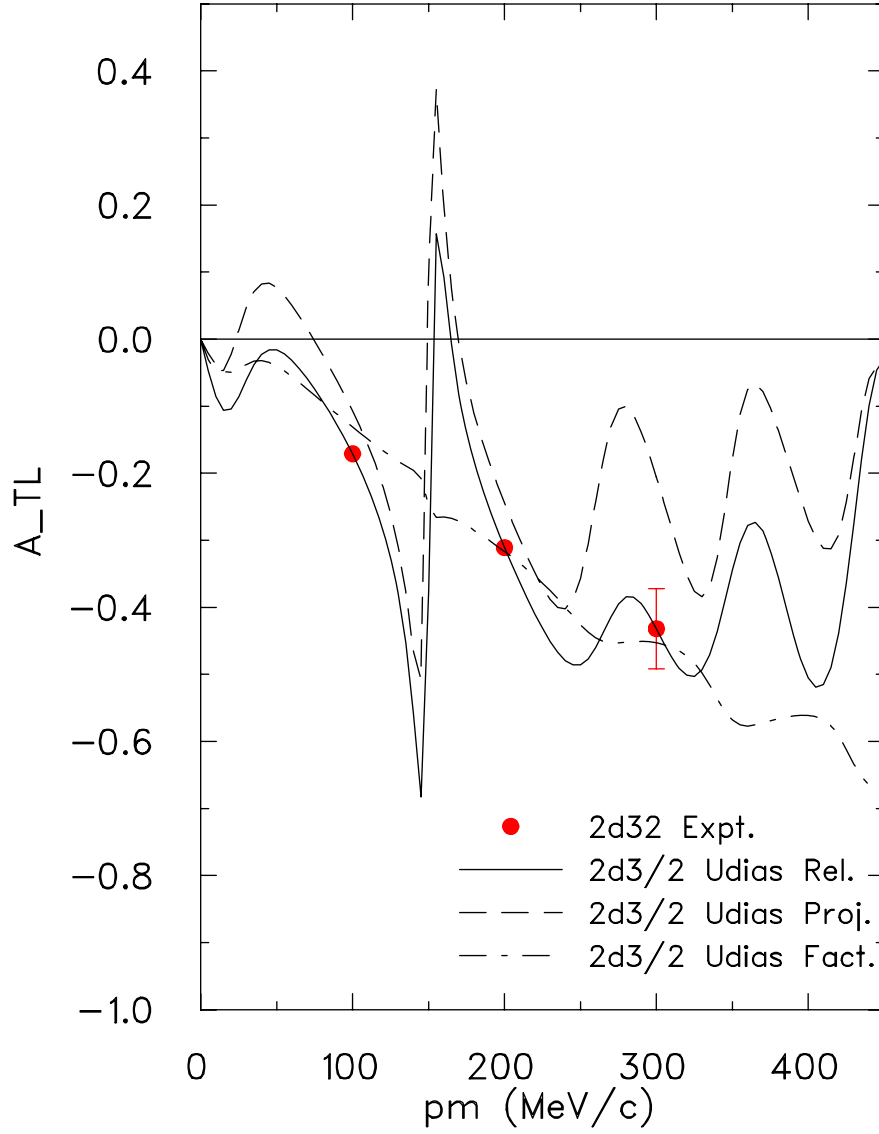


Figure 5.2: A_{TL} for the $2d_{3/2}$ 0.351 MeV state of ^{207}Tl . The experimental uncertainties are indicated at 100, 200 and 300 MeV/c. The meaning of the theoretical curves is described in the text.

$^{208}\text{Pb}(\text{e,ep})$ 1h11/2 A_{TL}

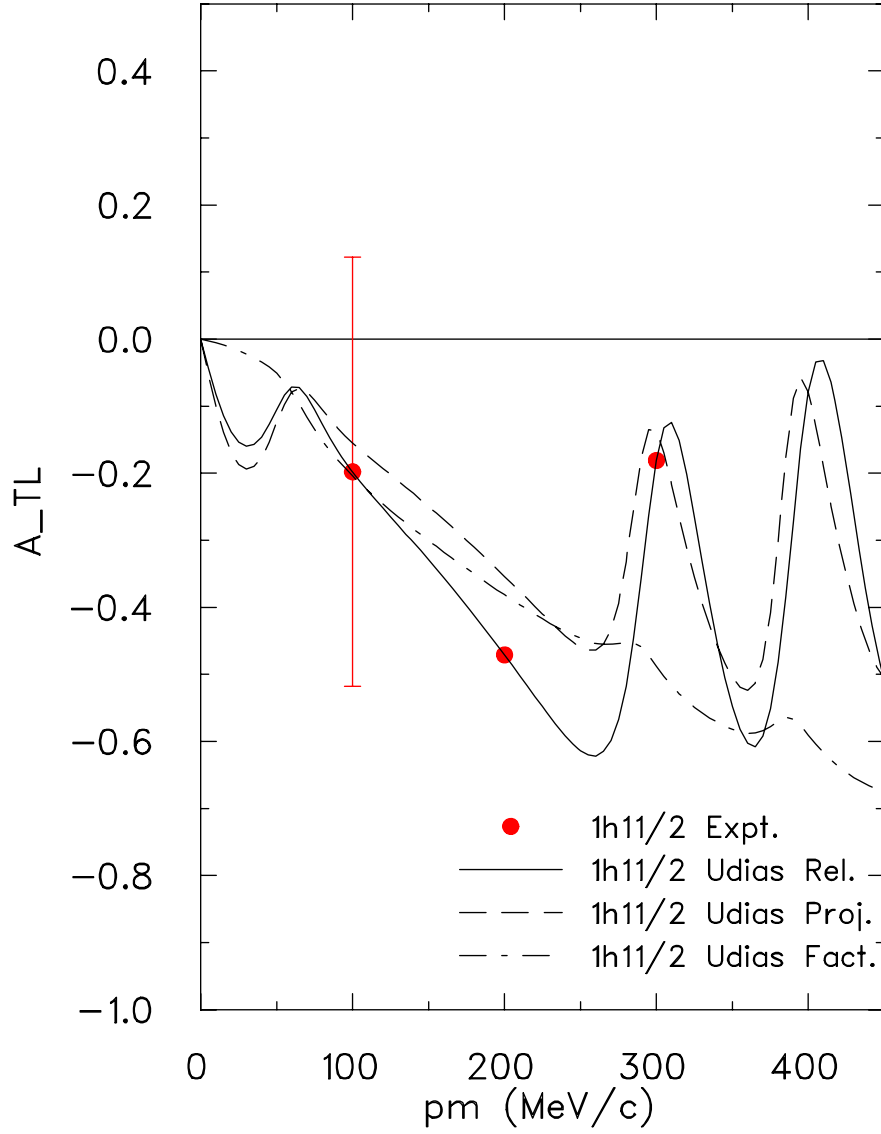


Figure 5.3: A_{TL} for the $1h_{11/2}$ 1.348 MeV state of ^{207}Tl . The experimental uncertainties are indicated at 100, 200 and 300 MeV/ c . The meaning of the theoretical curves is described in the text.

$^{208}\text{Pb}(\text{e,ep})$ 2d5/2 A_{TL}

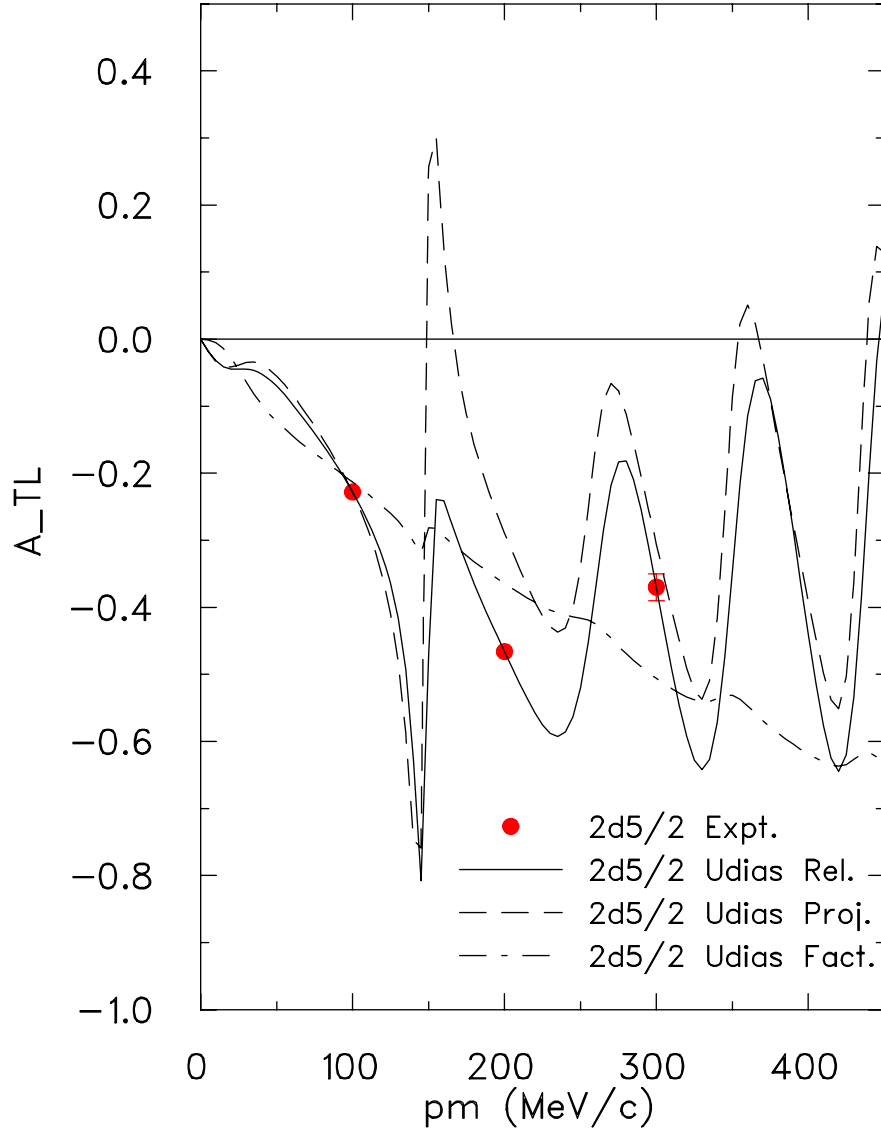


Figure 5.4: A_{TL} for the $2d_{5/2}$ 1.683 MeV state of ^{207}Tl . The experimental uncertainties are indicated at 100, 200 and 300 MeV/c. The meaning of the theoretical curves is described in the text.

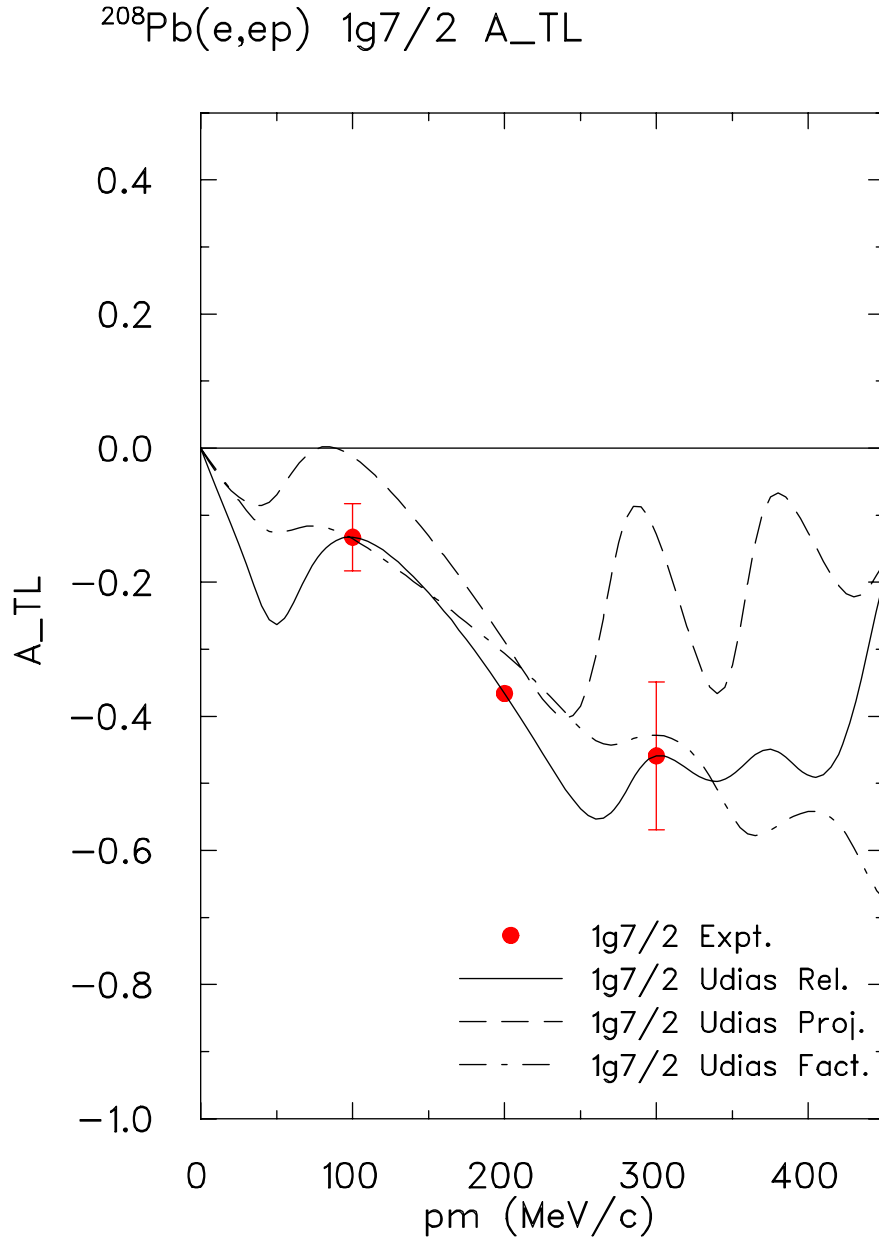


Figure 5.5: A_{TL} for the $1g_{7/2}$ 3.470 MeV state of ^{207}Tl . The experimental uncertainties are indicated at 100, 200 and 300 MeV/ c . The meaning of the theoretical curves is described in the text.

Chapter 6

Summary and Beam Time Request

6.1 Summary

(1) A new observable, A_{TL} , for the five low lying states of ^{207}Tl will be measured.

(2) The first measurements ever made in quasielastic kinematics on the paradigmatic shell model nucleus, ^{208}Pb at high Q^2 are proposed.

(3) Strength for $p_{miss} > 300 \text{ MeV}/c$ will give insight into nuclear structure issues and confront theoretical models.

6.2 Beam Time Request

We request 9 days of beam time to perform this experiment and make the necessary systematic measurements as shown in Table 6.1. The time estimates in Table 4.3, have been adjusted up by 30% to account for radiative losses. The table shows all necessary time, including the time to move the spectrometers.

We will perform an ARC and EP energy measurement, which takes ap-

Cross Section Measurements	180 hrs
Spectrometer Position Changes, Optics, and Bismuth run	32 hrs
ARC and EP Energy Measurements	4 hrs
Total	216 hrs (9 days)

Table 6.1: Time requested for the $^{208}\text{Pb}(e, e'p)^{207}\text{Tl}$ experiment.

proximately four hours. For each position of the spectrometers, we will take carbon pointing data. For these measurements we measure $^{12}\text{C}(e, e')$ and $^{12}\text{C}(e, e'p)$ from a multifoil carbon target. This allows us to calibrate the pointing of the spectrometers for each kinematical setting. This method has shown itself to agree with survey data while taking less time. They will also be valuable for obtaining an independent measurement of the absolute missing mass calibration. At forward angles we should be able to achieve good statistical accuracy and to resolve the ground state and first excited state of ^{11}B . The fitting procedure requires knowing the location of the excited states in the missing mass spectrum. The carbon data will be a good anchor for the missing mass calibration since the spectrometer momentum settings do not change with kinematical setting. The bismuth data will help establish the line shape profile and the missing mass spectrum calibration.

Appendix A

Kinematics

The kinematics for the $(e, e'p)$ reaction are shown in Figure A.1. The scattering plane is defined by the incoming electron, $e = (E_e, \mathbf{e})$, and the outgoing electron, $e' = (E_{e'}, \mathbf{e}')$. The four-momentum of the virtual photon is given by $q = (\omega, \mathbf{q})$ and the four-momentum of the outgoing proton is given by $p' = (E_p, \mathbf{p}')$. The four-momentum square, $Q^2 = q^2 - \omega^2$, is defined such that for electron scattering Q^2 is always positive. The missing momentum vector is defined as $\mathbf{p}_{miss} = \mathbf{q} - \mathbf{p}'$.

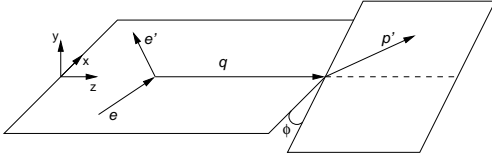


Figure A.1: A schematic of the kinematics for the $(e, e'p)$ reaction.

The form of the differential cross for $(e, e'p)$ reactions in the one-photon exchange approximation without polarization is:

$$\frac{d^6\sigma}{d\Omega_{e'}dE_{e'}d\Omega_{p'}dE_{p'}} = \frac{E_p p_p}{(2\pi)^3} \sigma_{Mott} [v_T R_T + v_L R_L + v_{TL} R_{TL} \cos \phi + v_{TT} R_{TT} \cos 2\phi], \quad (\text{A.1})$$

with ϕ the angle between the plane defined by \mathbf{e} and \mathbf{e}' and the plane defined by \mathbf{p}' and \mathbf{q} , σ_M is the Mott cross section,

$$\sigma_{Mott} = \frac{4\alpha^2 E_{e'}^2}{Q^4} \cos^2 \frac{\theta_{e'}}{2}. \quad (\text{A.2})$$

The kinematics factors v_L, v_T, v_{TL} , and v_{TT} are:

$$v_L = \frac{Q^4}{\mathbf{q}^4}, \quad (\text{A.3})$$

$$v_T = \frac{Q^2}{2\mathbf{q}^2} + \tan^2(\theta_e/2), \quad (\text{A.4})$$

$$v_{TL} = \frac{Q^2}{\mathbf{q}^2} \left[\frac{Q^2}{\mathbf{q}^2} + \tan^2(\theta_e/2) \right]^{1/2}, \text{ and} \quad (\text{A.5})$$

$$v_{TT} = \frac{Q^2}{2\mathbf{q}^2}. \quad (\text{A.6})$$

For the two body break-up channel, $^{208}\text{Pb}(e, e'p)^{207}\text{Tl}$, the proton energy and angle with respect to \mathbf{q} are correlated because the missing energy is fixed. In this case the differential cross is written as follows:

$$\frac{d^5\sigma}{d\Omega_{e'}d\Omega_{p'}dE_{e'}} = \frac{E_p P_p}{(2\pi)^3} \sigma_{Mott} f_{rec}^{-1} [v_T R_T + v_L R_L + v_{TL} R_{TL} \cos \phi + v_{TT} R_{TT} \cos 2\phi], \quad (\text{A.7})$$

where f_{rec} is the recoil factor,

$$f_{rec} = \left[1 - \frac{E_{p'}}{E_t} \frac{\mathbf{p}_m \cdot \mathbf{p}'}{p'^2} \right]. \quad (\text{A.8})$$

One can also measure the cross section asymmetry A_{TL} for a given \mathbf{q} and ω . This asymmetry is defined as:

$$A_{TL} = \frac{\sigma(\phi = 0) - \sigma(\phi = 180)}{\sigma(\phi = 0) + \sigma(\phi = 180)}. \quad (\text{A.9})$$

The cross section $\sigma(\phi = 0)$, forward of \mathbf{q} , is referred to as Σ_2 and $\sigma(\phi = 180)$, backward of \mathbf{q} , is referred to as Σ_1 .

$$x_B = \frac{Q^2}{2M\omega}, \quad (\text{A.10})$$

is the Bjorken scaling variable. For $x_B > 1$, the region in ω between the quasielastic peak and the elastic peak is being probed; while for $x_B < 1$, the region ω towards the delta peak is being probed. The region in ω between the quasielastic peak and delta peak is often referred to as the dip region.

Appendix B

Target Issues

B.1 Lead Target Test

We were able to run a test on a lead target design concept for 6 hours during development time. The kinematical conditions for the test are presented in Table B.1.

The target consisted of a stack of three lead foils placed in the 15 cm LH₂ beer can target. The 0.5 mm thick foils were placed 2.54 cm apart and oriented at 45° with respect to the beam. The upstream foil faced the full axial flow of the liquid hydrogen. The second and third foils were shadowed by the upstream foil. Singles and coincidence events (triggers 1,3,5) were recorded for the $^{208}\text{Pb}(e, e'p)$ reaction. Figure B.1 and Figure B.2 show the vertex location of the ep coincidences for the low current start of the test and high current end of the test respectively. It is clear that the two downstream foils suffered significant deterioration at the high current running.

Table B.2 shows the coincidence rate for the three foils using the ep coincidence trigger normalized to the original rate at 4.8 μA .

From these results it is clear that the upstream foil could withstand at least 60 μA . The raster during these tests only worked for the horizontal swing. We expect that if the full vertical and horizontal raster were used (4

$E_e(\text{MeV})$	$\omega(\text{MeV})$	$\theta_e(\text{deg})$	$\theta_p(\text{deg})$	$q(\text{MeV}/c)$	$p_m(\text{MeV}/c)$
2843.6	434.6	19.84	60.56	1001	101

Table B.1: Kinematical conditions for the lead target test.

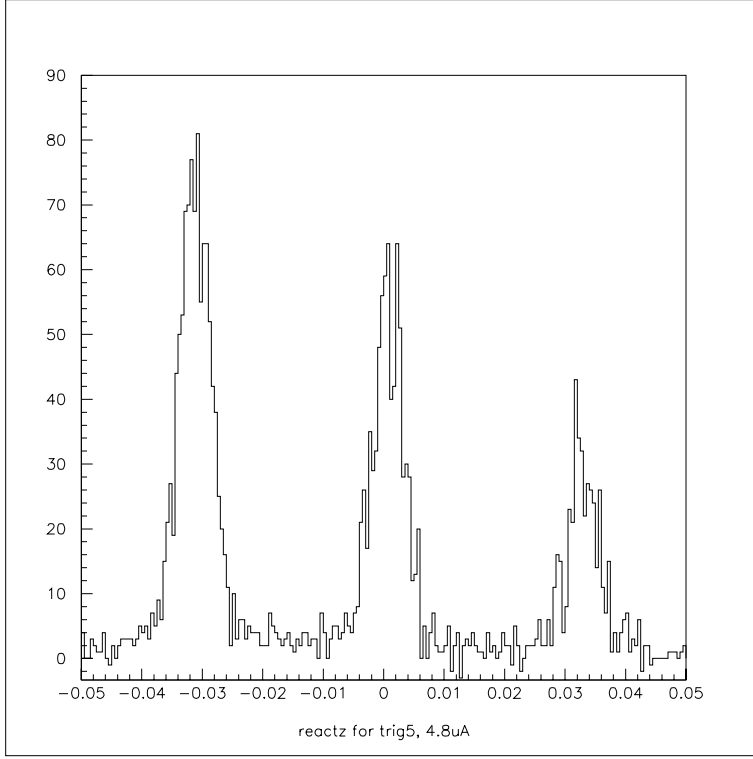


Figure B.1: react z for 3 foils at 4.8 μA start of test, run 1895

run	1895	1899	1900	1902	1903	1905	1906	1907
I (μA)	4.8	14.88	24.3	44.3	44.3	60	15.4	74.4
foil 1	1.00	1.00	1.00	1.060	1.040	1.020	0.970	0.860
foil 2	1.00	0.980	0.9630	0.890	1.010	1.050	0.810	0.050
foil 3	1.00	0.870	1.0	0.940	0.910	0.060	0.190	0.160

Table B.2: Lead Target Test using 3 Foils in 15 cm LH_2 Beer Can. Results per foil normalized to ep coincidence rate at run 1895.

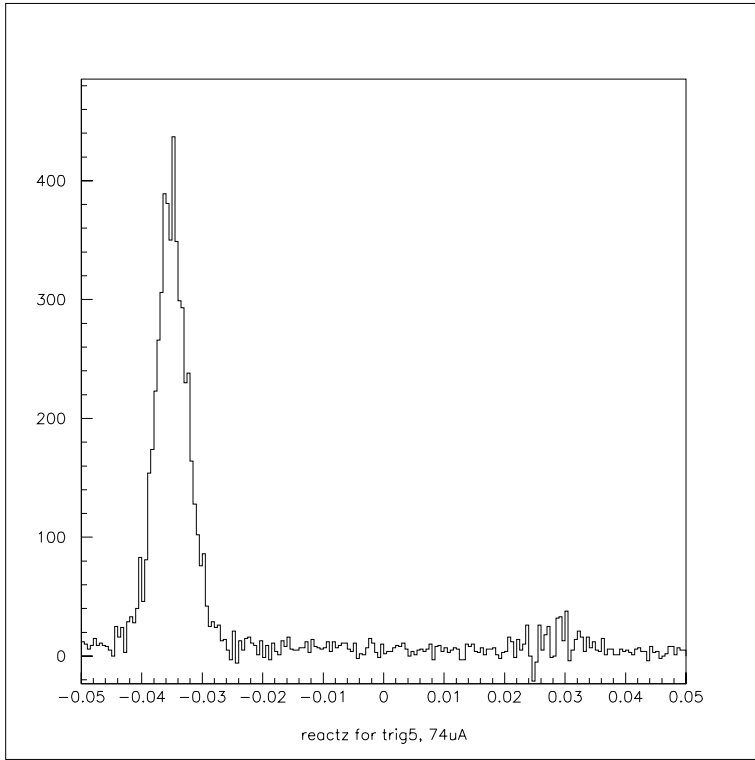


Figure B.2: react z for 3 foils at $74 \mu\text{A}$ at end of test, run 1907

state(MeV)	0	0.351	1.348	1.683	3.47
weight	1	2	0.29	5.1	0.63

Table B.3: Relative weights of the states excited in ^{207}Tl based on the theoretical predictions for $p_{\text{miss}} = 100 \text{ MeV}/c$.

mm x 4 mm) the forced cooling on the upstream foil could prevent the foil from deteriorating at currents higher than $60 \mu\text{A}$.

B.2 Target Development and Geant Simulations

B.2.1 Thin Target GEANT simulation in flowing LH_2

The aim of the experiment is to be able to measure the cross sections for individual low lying states of ^{207}Tl . In the case of the lead target test we ran a simulation to see what the spectrum should look like for the 0.5 mm lead foils in the beer can geometry. The GEANT spectrum is obtained by adding together the expected spectral shapes for the 5 states of ^{207}Tl at 0.0, 0.351, 1.348, 1.683 and 3.470 MeV according to the theoretical weights shown in Table B.3.

The GEANT spectra for these five states plus their weighted sum is shown in Figure B.3 for 0.02 MeV bins.

The simulation is realistic up to the spectrometer collimators. The effect of transport through the spectrometers is simulated by Gaussian smearing of momentum and angular resolution.

In order to investigate the effect of foil thickness and target geometry we also ran a GEANT simulation using a 0.1 mm thick lead target in a vertically flowing LH_2 stream. The total LH_2 path length along the beam is 6 cm.

The missing mass spectrum for this simulation is shown in Figure B.4.

We ran GEANT a second time for the same geometry and kinematics but with different random number seeds. If we treat the first run as data and the second run as simulation we can get a measure of the best result we can expect in unfolding the missing mass spectra to extract the individual peaks. The data spectrum assumes very good statistical accuracy. The result of this exercise is shown in Table B.4.

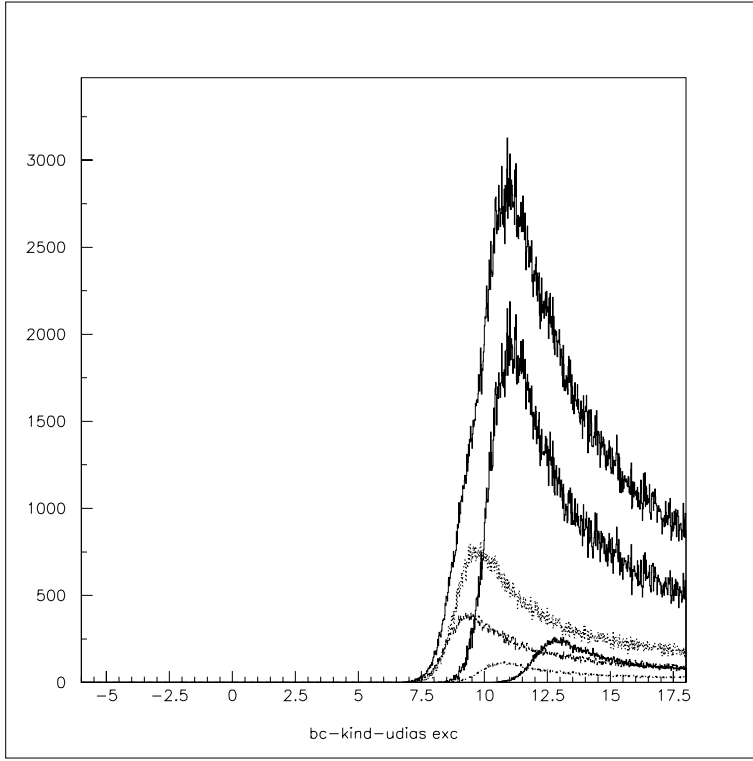


Figure B.3: GEANT simulations of the five states of ^{207}Tl excited with the weights in Table B.3 for the beer can geometry and 0.5 mm thick lead foils. The spectrum is for the upstream foil.

state	weight	input cnts	extracted cnts	input/extracted
0	1	258891	262885	0.980
0.351	2	512726	507461	1.010
1.348	0.29	72116	77773	0.930
1.683	5.1	1252055	1244637	1.010
3.47	0.63	142447	144510	0.990

Table B.4: A comparison of two separate GEANT simulations of the 0.1 mm Pb foil placed in the 6 cm long LH_2 environment. The first simulation is the input. The second simulation extracts the number of counts from a fit to the summed spectrum of the first simulation. The two simulations used different random number seeds.

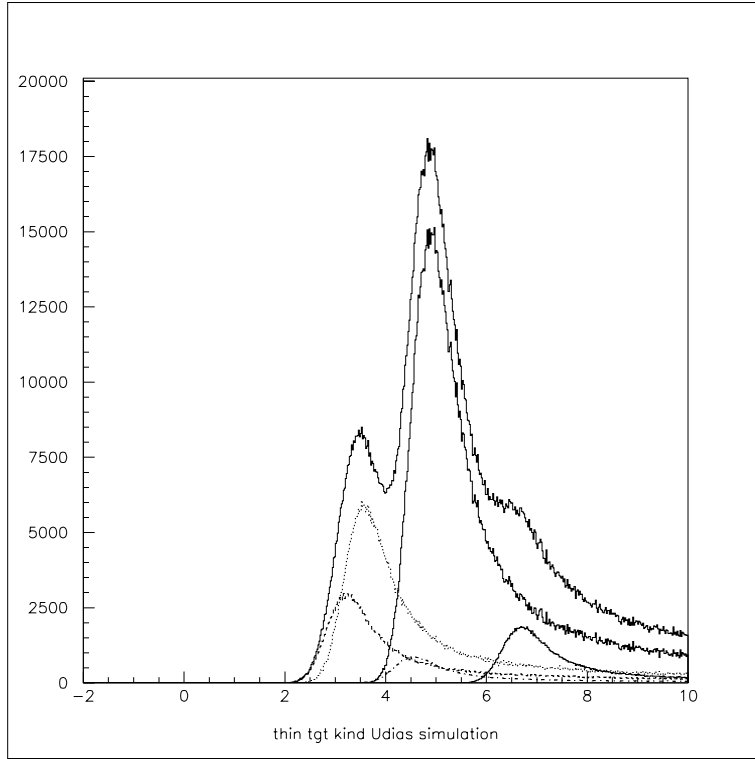


Figure B.4: GEANT simulations of the five states of ^{207}Tl excited with the weights in Table B.3 for the thin 0.1 mm lead target in a flowing LH_2 stream of total length 6 cm. This figure should be compared to the simulation of the beer can target, Figure B.3, used in the test run

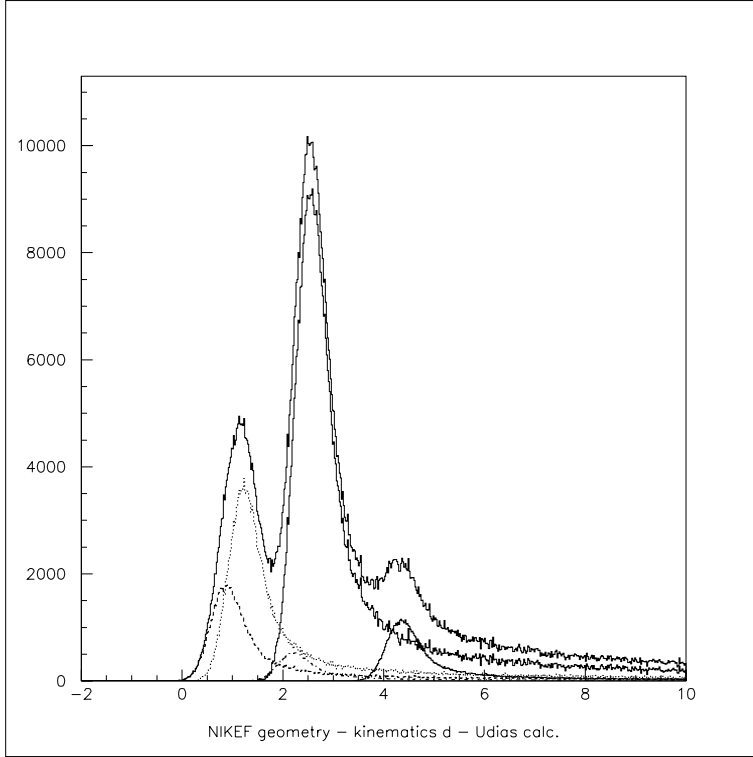


Figure B.5: GEANT simulations of the five states of ^{207}Tl excited with the weights in Table B.3 for the NIKHEF geometry consisting of two thin foils of ^{208}Pb , 0.038 mm each, separated by 5 mm. Spectra are generated from scattering from the down stream foil. Kinematics correspond to the target test run discussed in the text. See Table B.1.

B.2.2 Simulation using the NIKHEF Geometry

GEANT was used to simulate the missing mass spectrum expected from the lead target test had we used the NIKHEF geometry [5]. This configuration had no other material in the beam path besides two thin (0.038 mm) lead foils separated by 5 mm. The simulated missing mass spectrum uncorrected for energy loss is shown in Figure B.5.

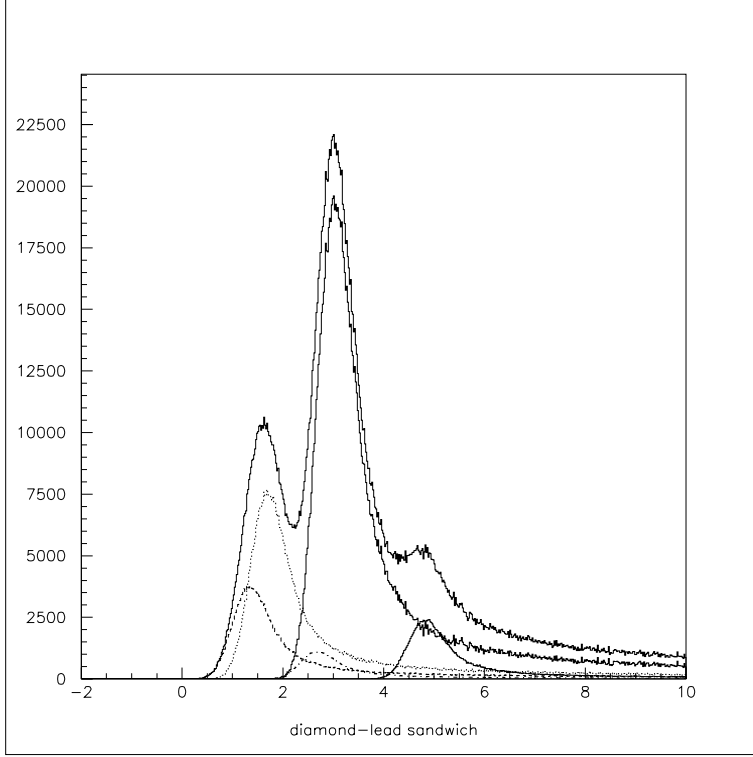


Figure B.6: Simulated missing mass spectrum for a diamond-lead-diamond sandwich for a 0.1 mm thick lead foil and 0.15 mm thick diamond foils

B.2.3 Simulation using a Diamond-Lead Foil Sandwich

Preparations for conditionally approved experiment E03-011 have demonstrated that cold lead-diamond sandwiches can withstand currents up to $80 \mu\text{A}$ and calculations indicate that they can operate at $100 \mu\text{A}$. The sandwich consists of a lead foil of 0.5 mm thickness placed between two diamond foils of thickness 0.15 mm each. At cryogenic temperatures the thermal conductivity of diamond is very large. A description of the target and test is found in [35]. The Q-values for $^{12}\text{C}(e, e'p)^{11}\text{B}$ and $^{13}\text{C}(e, e'p)^{12}\text{B}$ are -16 Mev or higher. This leaves the ^{207}Tl spectrum clear of carbon generated contaminants in the excitation region of interest. GEANT simulations of the expected missing mass resolution with a 0.1 mm thick lead foil for this geometry for $p_{\text{miss}} = 100\text{MeV}/c$ are shown in Figure B.6.

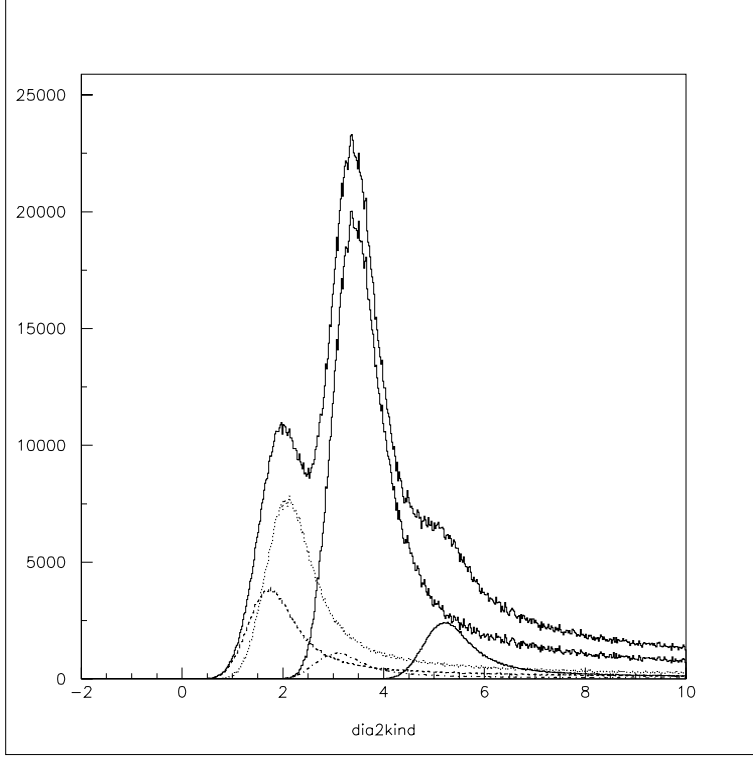


Figure B.7: Missing mass spectrum for a diamond/lead/diamond sandwich for 0.2 mm thick lead. Compare to Figure B.6

A lead foil thickness of 0.1 mm requires a very long running time to obtain useable numbers of events. In order to determine the effect of the lead thickness on our ability to extract the peak areas we also ran the simulation for $p_{miss} = 100\text{MeV}/c$ for a lead thickness of 0.2 mm. This is shown in Figure B.7.

At higher missing momentum the cross section falls rapidly. In order to estimate our ability to extract the peak areas of the states in the excitation energy spectrum we also ran simulations with the expected experimental counts. This is important for obtaining the uncertainties in the asymmetry, A_{TL} . The results from the fits are shown in Table 5.1.

The spectrum and fit for the case of kin05 from Table 4.3 is shown in Figure B.8.

From the lead target test and the simulations we conclude that we have at present two viable high current targets, the cryogenic diamond-foil-lead

sandwich and the 0.2 mm lead foil in a LH₂ flowing stream with a short liquid hydrogen path. The principle factor in the quality of the fitting result is the number of events to be fitted. A secondary factor is the resolution. During our simulations we also tried using a 0.5 mm foil. This thickness foil washes out the peaks altogether, for example Figure B.3. However, what is lacking in resolution can be compensated for by more counts in the spectrum. Even though the individual peaks are not always visible their areas can be extracted given sufficient counts. In order for this to be successful, however, we will need to know the energy calibration rather well. A lead target thickness of 0.2 mm seems to be a good compromise between resolution and number of counts.

B.2.4 Calibration of Missing Mass Spectrum with Bismuth

The simulations reveal that peak extraction is possible even for modest counts provided that we know the line profile. It would be preferable if we had an experimental line shape. We can come close to this by using a bismuth target exploiting the $^{209}\text{Bi}(e, e'p)^{208}\text{Pb}$ reaction. The first excited state of ^{208}Pb is at 2.6 MeV and so the ground state is clear of overlapping nearby states. The Q-value for the bismuth reaction is also favorable, being even farther away from the carbon Q-value for $^{12}\text{C}(e, e'p)^{11}\text{B}$, which is -15.96 MeV, than is lead. Bismuth has a lower melting point by 50°C than lead, so the target prepared for lead would be the same as that for bismuth. This is summarized in Table B.5 for which the target thickness of bismuth was chosen to be the same fractional radiation length as that for the lead target.

The ground state of ^{209}Bi is believed to be $1h_{9/2-}$. We expect the cross section for the $^{209}\text{Bi}(e, e'p)^{208}\text{Pb}$ reaction to be maximum at missing momentum of 200 MeV/ c . A run of about 12 hours would give about 0.5M counts, which is equivalent to the counts we used in the GEANT simulations to establish the line profile.

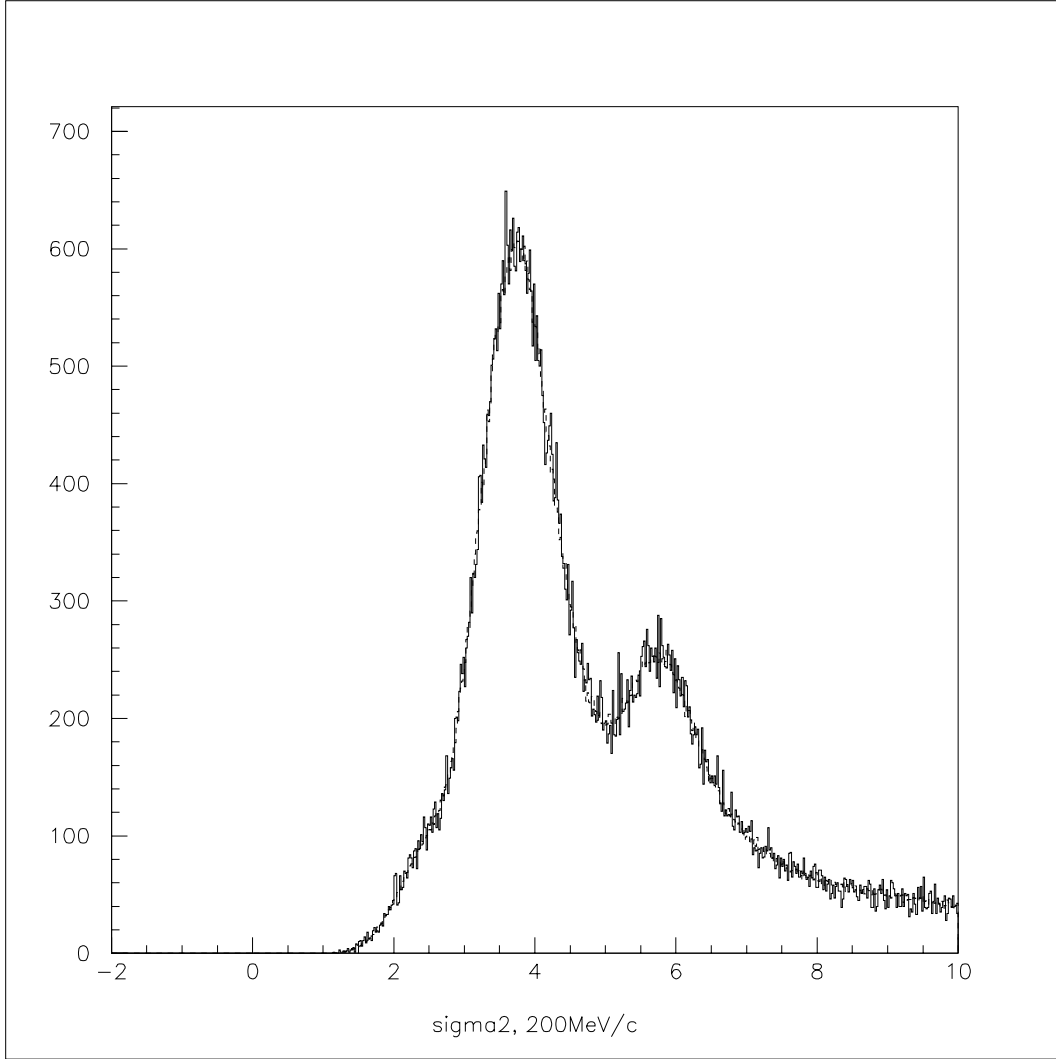


Figure B.8: GEANT simulation and fit of the raw excitation energy spectrum for $p_{miss} = 200 \text{ MeV}/c$ using the expected counts for the Σ_2 kinematics (kin05) in Table 4.3.

	Pb	Bi
t (cm)	0.02	0.023
$X_0(\text{g}/\text{cm}^2)$	6.37	6.29
$\rho(\text{g}/\text{cm}^3)$	11.35	9.747
$\rho t (\text{g}/\text{cm}^2)$	0.227	0.224
$\rho t/X_0$	0.0356	0.0356
dE/dx (Mev/g/cm ²)	1.6	1.6
dE _p (MeV)	0.36	0.36
dE _e (MeV)	0.45	0.45
Q-value ($e, e'p$), (MeV)	-8.01	-3.80

Table B.5: A comparison of a Pb target and Bi if they both have the same fraction of radiation length

Bibliography

- [1] W. Bertozzi, K. Fissum, A. Saha, and L. Weinstein. Study of the Quasielastic (e,e'p) Reaction in ^{16}O at High Recoil Momentum. E89003 Jefferson Lab Experiment.
- [2] K.I. Blomqvist et al. *Zeitschrift fur Physik A*, 351:353, 1995.
- [3] Liyanage and The Jefferson Lab Hall A Collaboration. Dynamics of the $^{16}\text{O}(e, e'p)$ reaction at high missing energies. *Physical Review Letters*, 86:5670, 2001.
- [4] J. Gao and The Jefferson Lab Hall A Collaboration. Dynamical relativistic effects in quasielastic 1p-shell proton knockout from ^{16}O . *Physical Review Letters*, 84:3265, 2000.
- [5] I. Bobeldijk et al. High-momentum protons in ^{208}Pb . *Physical Review Letters*, 73:2684, 1994.
- [6] L. Lapikas, G. van der Steenhoven, L. Frankfurt, M. Strikman, and M. Zhalov. *Physical Review C*, 61:064325, 2000.
- [7] L. Frankfurt, M. Strikman, and M. Zhalov. *Physics Letters B*, 503:73, 2001.
- [8] H. Müther and I. Sick. Correlated nucleons in configuration space. *Physical Review C*, 70:041301R, 2004.
- [9] J.M. Udias, J.A. Caballero, E. Moya de Guerra, Javier R. Vignote, and A. Escudero. Relativistic mean field approximation to the analysis of $^{16}\text{O}(e, e'p)^{15}\text{N}$ data at $|Q^2| \leq 0.4(\text{Gev}/c)^2$. *Physical Review C*, 64:024614, 2001.
- [10] L. Chinitz et al. *Physical Review Letters*, 67:568, 1991.

- [11] C.M. Spaltro et al. *Physical Review C*, 48:2385, 1993.
- [12] M. Leuschner et al. *Physical Review C*, 49:955, 1994.
- [13] E. Quint. *Limitations of the mean-field description for nuclei in the Pb-region, observed with the (e,e'p) reaction*. PhD thesis, Universiteit van Amsterdam, March 15 1988. unpublished, NIKHEF-K Nr.1313.
- [14] Marcel van Batenburg. *Deeply-bound protons in ^{208}Pb* . PhD thesis, University of Utrecht, 05 March 2001. unpublished, Ph. D. thesis.
- [15] J.M. Udias, P. Sarriguren, E. Moya de Guerra, E. Garrido, and J.A. Caballero. Spectroscopic factors in ^{40}Ca and ^{208}Pb from (e,e'p): Fully relativistic analysis. *Physical Review C*, 48:2731, 1993.
- [16] J.M. Udias, P. Sarriguren, E. Moya de Guerra, E. Garrido, and J.A. Caballero. Relativistic versus nonrelativistic optical potentials in A(e,e'p)B reactions. *Physical Review C*, 51:3246, 1996.
- [17] E.D. Cooper et al. *Physical Review C*, 36:2170, 1987.
- [18] J.M. Udias, P. Sarriguren, E. Moya de Guerra, and J.A. Caballero. Relativistic analysis of the $^{208}\text{Pb}(e,e'p)^{207}\text{Tl}$ reaction at high momentum. *Physical Review C*, 53:1488, 1996.
- [19] James J. Kelly. Effects of spinor distortion and density-dependent form factors upon $^{16}\text{O}(\vec{e}, e'\vec{p})$. *Physical Review C*, 60:044609, 1999.
- [20] J. A. Caballero, T. W. Donnelly, E. Moya de Guerra, and J. M. Udias. Relativistic current densities for bound spin-orbit partners and the longitudinal-transverse response in (e,e'p) processes. *Nuclear Physics A*, 643:189, 1998.
- [21] J.M. Udias, Javier R. Vignote, E. Moya de Guerra, A. Escuderos, and J.A. Caballero. Recent developments in relativistic models for exclusive (e,e'p) reactions. Proceedings of the 5th Workshop on e.-m. induced two-hadron emission, Lund, June 13-16, 2001, nucl-th/0109077.
- [22] J.M. Udias, J.A. Caballero, E. Moya de Guerra, J.E. Amaro, and T.W. Donnelly. Quasielastic scattering from relativistic bound nucleons: Transverse-longitudinal response. *Physical Review Letters*, 83:5451, 1999.

- [23] H. Mütter and W. H. Dickhoff. *Physical Review C*, 49:R17, 1994.
- [24] Z.Y. Ma and J. Wambach. *Physics Letters B*, 256:1, 1991.
- [25] W. Bertozzi, K. Fissum, A. Saha, and L. Weinstein. Testing the limits of the Single Particle Model in $^{16}\text{O}(e, e'p)$: An update to E89-003. Jefferson National Accelerator Facility experiment E00-102.
- [26] J.E. Amaro, M.B. Barbaro, J.A. Caballero, and F. Kazemi Tabatabae. Semi-relativistic meson exchange currents in (e, e') and $(e, e'p)$ reactions. *Physical Review C*, page 014604, 2003.
- [27] K. Fissum and The Jefferson Lab Hall A Collaboration. The dynamics of the quasielastic $^{16}\text{O}(e, e'p)$ reaction at $Q^2 = 0.8 \text{ (GeV/c)}^2$. *Physical Review C*, 70:034606, 2004.
- [28] Javier R. Vignote, R. Álvarez-Rodríguez, C. Fernández-Ramírez, E. Garrido, E. Moya de Guerra, and J.M. Udías. Recent developments in relativistic models for exclusive $A(e, e'p)B$ reactions. Proceedings of the Twenty Third International Workshop on Nuclear Theory, Rila, June 14-19 2004.
- [29] J. Alcorn and the Jefferson Hall A Collaboration. *Nuclear Instruments and Methods in Physics Research A*, 522:294, 2004.
- [30] M.M. Rvachev et al. Quasielastic $^3\text{He}(e, e'p)^2\text{H}$ reaction at $Q^2 = 1.5 \text{ GeV}^2$ for recoil momenta up to 1 GeV/c . *Physical Review Letters*, 94:192302, 2005.
- [31] K. Aniol, S. Gilad, D. Higinbotham, and A. Saha, 2004. Jefferson National Accelerator Facility, approved experiment, E04-107.
- [32] private communication, J. M. Udias.
- [33] J. W. Lightbody and J. S. O'Connell. *Computers in Physics*, 57, May/June 1988.
- [34] private communication, A. Saha.
- [35] R. Michaels, P. Souder, and G. Urciuoli. Neutron Skin of ^{208}Pb through Parity Violating Electron Scattering., 2003. Jefferson National Accelerator Facility, conditionally approved experiment E03-011.